Nature Communications

https://doi.org/10.1038/s41467-026-72803-z

Article in Press

Nanoparticle-enabled tuning of cell density for enhanced adhesion and tissue repair

Received: 23 October 2025

Accepted: 24 April 2026

[redacted]

Cite this article as: Park, H.S., Im, G.-B., Jeong, S.Y. *et al.* Nanoparticle-enabled tuning of cell density for enhanced adhesion and tissue repair. *Nat Commun* (2026). https://doi.org/10.1038/s41467-026-72803-z

Hyun Su Park, Gwang-Bum Im, So Yun Jeong, Jongseok Lee, Amélie Ferran, Jihyun Lee, Sung-Won Kim, Jiyu Hyun, Young-Ju Jang, Eun-Cheol Lee, Younghoon Lee, Jong Wook Bae & Suk Ho Bhang

We are providing an unedited version of this manuscript to give early access to its findings. Before final publication, the manuscript will undergo further editing. Please note there may be errors present which affect the content, and all legal disclaimers apply.

If this paper is publishing under a Transparent Peer Review model then Peer Review reports will publish with the final article.

ARTICLE IN PRESS

© The Author(s) 2026. **Open Access** This article is licensed under a Creative Commons Attribution-NonCommercial-NoDerivatives 4.0 International License, which permits any non-commercial use, sharing, distribution and reproduction in any medium or format, as long as you give appropriate credit to the original author(s) and the source, provide a link to the Creative Commons licence, and indicate if you modified the licensed material. You do not have permission under this licence to share adapted material derived from this article or parts of it. The images or other third party material in this article are included in the article's Creative Commons licence, unless indicated otherwise in a credit line to the material. If material is not included in the article's Creative Commons licence and your intended use is not permitted by statutory regulation or exceeds the permitted use, you will need to obtain permission directly from the copyright holder. To view a copy of this licence, visit http://creativecommons.org/licenses/by-nc-nd/4.0/.

Nanoparticle-enabled tuning of cell density for enhanced adhesion and tissue repair

Hyun Su Park[1,#], Gwang-Bum Im[2,3,#], So Yun Jeong[1], Jongseok Lee[4], Amélie Ferran[5], Jihyun Lee[6], Sung-Won Kim[1], Jiyu Hyun[1], Young-Ju Jang[1], Eun-Cheol Lee[1], Younghoon Lee[7], Jong Wook Bae[1,*], Suk Ho Bhang[1,*]

[1]*School of Chemical Engineering, Sungkyunkwan University, Suwon 16419, Republic of Korea*

[2]*Department of Cardiac Surgery, Boston Children's Hospital, Boston, MA, USA*

[3]*Department of Surgery, Harvard Medical School, Boston, MA, USA*

[4]*Department of Mechanical Engineering, Gachon University, Seongnam 13420, Republic of Korea*

[5]*Department of Energy and Process Engineering, Norwegian University of Science and Technology, Trondheim NO-7491, Norway*

[6]*Division of Engineering in Medicine, Department of Medicine, Brigham and Women's Hospital, Harvard Medical School, Boston, MA 02115, USA*

[7]*Department of Mechanical Engineering, Kyung Hee University, Yongin 17104, Republic of Korea*

# These authors contributed equally to this work

***Authors to whom correspondence should be addressed.**

E-mail: *sukhobhang@skku.edu* and *finejw@skku.edu*

Abstract

Low retention of transplanted stem cells at target sites remains a major barrier to the clinical translation of cell-based therapies. Conventional strategies, including genetic modification, chemical functionalization, and biomaterial encapsulation, often face limitations in translational feasibility, safety, or procedural complexity. Here, we present a nanoparticle-enabled biophysical approach to enhance cell retention. We incorporate cell-settling nanoparticles composed of clinically approved materials into mesenchymal stem cells, increasing cellular density to accelerate gravitational settling and improve adhesion and survival. Building on this, we develop copper-chaperone-activatable nanoparticles, which enhance tissue regeneration and anti-fibrotic signaling through activation of fibroblast growth factor 2 and a positive feedback loop. In a mouse skin wound model, we show that copper-chaperone-activatable nanoparticle-treated mesenchymal stem cells exhibit enhanced vascularization and reduced fibrosis. These findings demonstrate that modulation of cellular density and physical forces can improve stem cell engraftment, establishing a biophysical framework for safe and translationally relevant cell-based therapies.

Introduction

Recent advances in stem cell therapy have faced persistent challenges in achieving adequate cell retention at target sites, which significantly limits therapeutic effectiveness[1–3]. Despite extensive efforts to use various types of stem cells for clinical applications, the major limiting factor remains the low engraftment and retention of transplanted cells at the injury site[4]. In particular, previous research reports have identified this issue as a significant obstacle for mesenchymal stem cells (MSCs), which are known to be remarkably effective in tissue regeneration and disease treatment through the secretion of healing substances and immune regulation[5,6] . While cell retention enhancement strategies such as genetic engineering and chemical functionalization have been proposed[7–11], they present complicated regulatory, unpredictable cellular responses, and safety concerns associated with direct molecular manipulation, hindering clinical translation[12–14]. In parallel, biomaterial-based approaches to enhance cell retention include hydrogel encapsulation, cell sheet or tissue patch formation, and magnetic nanoparticle–assisted targeting using external magnetic fields[15–18] . Although these approaches can improve local retention, these methods often require additional materials, invasive procedures, or external devices. These considerations led us to explore a more straightforward approach aimed at improving the safety and local retention of transplanted cells while maintaining procedural simplicity.

Physical forces such as gravity and buoyancy are fundamental, yet underexplored factors that significantly influence the retention and adhesion of stem cells in wound environments[19–22]. Incorporating techniques that can manipulate these forces through biophysical strategies into stem cells could offer a promising avenue for enhancing their therapeutic efficacy without the need for genetic or chemical manipulation. Gravitational and buoyant forces play crucial roles in various biological contexts such as embryonic development, tissue morphogenesis, and wound healing, where dynamic control of cell positioning, settling, and adhesion is essential[23,24]. Changes in cell buoyancy and density during processes such as differentiation and mitosis further impact cell interactions with their environment[25]. Especially in wound sites, where exudate fluid exhibits a higher density than standard culture media, stem cells must respond to and overcome resistive forces to attach effectively to extracellular matrices or host tissues[26–28]. As delays or defects in attachment can lead to cell death and impaired tissue health[29,30], this is crucial. However, the impact of density changes on cellular function remains poorly understood, particularly their influence on adhesion and other density-sensitive traits[31]. Addressing this gap is critical for advancing biophysical strategies that improve stem cell retention in clinically relevant settings. This study aimed to introduce a translationally relevant biophysical platform that enhances stem cell retention and therapeutic efficacy by modulating cellular density through the use of functionalized nanoparticles, thereby promoting accelerated settling, improved adhesion, and amplified regenerative signaling in challenging wound environments.

To address the challenges, we developed cell-settling nanoparticles (CN) based on clinically approved materials, combining biophysical engineering approaches (**Fig. 1**). These nanoparticles are rapidly incorporated into mesenchymal stem cells (MSCs), resulting in increased intracellular mass and density. While this mass increase accelerates gravitational sedimentation *in vitro*, improving MSC adhesion to surfaces and enhancing cell viability (**Fig. 1a**), nanoparticle-based strategies incorporating degradable specific metals have also been demonstrated to improve the therapeutic efficacy of cells significantly (**Fig. 1b**). These biophysical engineering approaches could provide a more direct path toward clinical applications by inducing enhanced stem cell attachment, survival, and therapeutic potential through control of cell mass and density, while avoiding the regulatory complexities associated with genetic and chemical interventions. Building upon this platform, copper-chaperone-activatable cell-settling nanoparticles (CCN) were introduced to further elevate fibroblast growth factor 2 (FGF2) expression through a positive feedback loop, thereby stimulating both cell aggregation and regenerative pathways. An *in vivo* mouse skin wound model was applied to demonstrate that administration of CCN-engineered MSCs significantly enhanced vascularization and suppressed fibrotic scarring compared to controls, consistent with recent findings highlighting MSCs' dual role in promoting vascularization and combating pathological fibrosis. Together, our approach redefines nanoparticles beyond conventional delivery vehicles, establishing them as physical levers of cell behavior through density tuning.

Results

Effect of CN to cellular physical properties

First, we fabricated CN and introduced it to MSCs to increase the individual cell density and adhesive efficiency (**Fig. 2a and Fig. S1**). The one-pot synthesized silica-based-CN showed a uniform diameter of approximately 35 nm (**Fig. 2b**). Tissue culture-treated plates are surface-modified by corona discharge or gas plasma treatment, which leaves the surface hydrophilic and negatively charged upon the addition of media[32,33]. Therefore, to minimize the electrostatic interactions of CN with the cell surface and isolate the effects of density, we designed CN with a negative zeta potential, in contrast to positively charged nanoparticles (**Fig. S2a**). CN exhibited remarkably low cytotoxicity when treated at a concentration of 400 μg/mL to MSCs (**Fig. 2d**). Fifteen minutes after the CN treatment, CN was successfully internalized to MSCs (**Fig. 2c**).

Correspondingly, side scatter (SSC)-based cellular complexity was enhanced by approximately 1.7-fold compared to the NT group (**Fig. S2b**). During the process of nanoparticle incorporation into cells, cellular weight was significantly increased along with the change in individual cell density, as calculated by fluorescence intensity and dry mass measurements (**Fig. 2e and Fig. S2e**). Increased cell density can reduce buoyant time due to increased gravitational force, which is simulated using the equation, $d(x)=2/9\cdot((\rho p-\rho f)gr^{2})/\eta\cdot t$ (**Fig. 2f,g and Fig. S2e**). To confirm the sedimentation rate with increased cell density, we utilized a cell separation and FACS complex system after distinguishing the PE-positive NT group and CN-incorporated cells (**Fig. 2h,i and Fig. S2c**). With increased cell settling speed, the time-dependent cell population was four-fold higher in the CN group (**Fig. 2i**). Also, CN-incorporation increased the cell attachment efficiency after seeding MSCs to the cell culture plate (**Fig. 2j,k, and Fig. S2d**).

Development of CN to CCN for copper chaperone activation

As our previous Cu-based system increased copper chaperone transfer efficiency and activated vascularization[34], we applied Cu to the CN system to strengthen the therapeutic efficacy of MSCs. To induce copper chaperone activation without changing CN incorporation property, we optimized a one-pot synthesis to coat copper onto the present CN system (**Fig. 3a and Fig. S1**). After the synthesis, copper on the surface of CCN and surface area were investigated compared to CN with various methods such as XRD, XRF, TEM images, and Zeta-potential analysis (**Fig. 3b** and **Fig. S3a-d**). While the changes of surficial composition in CCN, the improvement in cell complexity and cell adhesive efficiency were similar between CN and CCN groups (**Fig. 3c-e**). In addition, the increased cellular density, achieved through both CN and CCN, accelerated cell sinking speed

(**Fig. S2f, g**). After cell adhesion, various adhesion-related gene and protein expressions, including CD44, N-cadherin, and integrin α5, were significantly increased in both CN and CCN groups (**Fig. 3f and Fig. S3e**). As CN and CCN with negative zeta-potential have a low effect on the surface hydrophilicity and cell adhesive efficiency, there was less possibility that the effect of particles near the dish surface would impact the cell adhesion (**Fig. S3f-i**). Therefore, we concluded that the incorporated weight of CN or CCN strongly affected cell adhesion efficiency (**Fig. 2 and 3**). Mechanistically, CN induces predominantly biophysical settling effects, whereas CCN integrates both biophysical and biochemical mechanisms. Based on these results, we aimed to investigate the effects of enhanced cell sinking speed by injecting CN or CCN-integrated cells into *in vivo* experiments. We confirmed that retention at the wound site was improved when CN or CCN was applied (**Fig. 3g, h**). The ratio of human GAPDH to mouse β-actin was markedly increased in both groups (**Fig. S3i**), accompanied by elevated *Vegf*, *Fgf2*, and *Mki67* expression (**Fig. S3j**), consistent with enhanced engraftment and regenerative signaling. To directly distinguish copper-mediated biochemical effects from nanoparticle-driven physical density modulation, we compared CCN with soluble copper salt controls ($CuCl_2$ and $CuSO_4$) by assessing cell viability **(Fig. S3k**). While exposure to soluble copper salts resulted in reduced viability, CCN-treated cells maintained significantly higher viability under equivalent copper conditions. These findings indicate that the nanoparticle formulation mitigates copper-associated cytotoxicity and supports cell survival compared with soluble copper alone. To further evaluate potential off-target or inflammatory effects following transplantation, we transplanted MSCs loaded with CN or CCN into a mouse skin wound model and assessed tissue responses at day 14 **(Fig. S4)**. Histological analyses of major organs, including the liver, lung, and spleen, showed no evidence of fibrosis or pathological remodeling (**Fig. S4a,c,e**). In addition, detection of human GAPDH in the transplanted tissues showed no substantial differences in gene expression compared with negative control groups, further indicating the absence of aberrant off-target persistence or unintended systemic distribution (**Fig. S4b,d,f**). To examine the persistence and potential degradation of CN/CCN, we performed Cryo-TEM analyses on day 14 and compared them with day 3 samples. (**Fig. S5a**). Relative to day 3, intracellular nanoparticle content was remarkably reduced by day 14, consistent with substantial degradation and/or clearance of CN/CCN over time (**Fig. S5b**). These observations are in line with the known biodegradability of silica-based nanoparticles and suggest that the nanoparticles used in this study do not persist indefinitely within MSCs. Furthermore, as no significant differences were observed in the number of F4/80$^+$ macrophages at the wound site on day 14, we did not detect any notable adverse effects related to off-target responses or inflammation under the conditions tested (**Fig. S5c,d**). Importantly, CN/CCN loading did not compromise intrinsic MSC properties in vitro. MSCs maintained robust proliferative capacity over several days, and notably, CCN-treated MSCs exhibited enhanced proliferation compared to untreated controls (**Fig. S5e**). Expression of canonical MSC markers (e.g., CD90 and CD105), assessed by quantitative PCR, remained unchanged following nanoparticle incorporation, confirming preservation of MSC identity at the transcriptional level (**Fig. S5f,g**). During MSC culture, we hypothesized that CCN-mediated enhancement of MSC proliferation might be associated with the upregulation of pro-angiogenic and wound regenerative factors. To test this possibility, we examined two representative mediators, FGF2 and VEGF. Among the angiogenic and regenerative factors analyzed, FGF2 expression was significantly increased following CCN treatment, whereas VEGF did not exhibit measurable differences at the protein level between groups (**Fig. S5h**). These findings suggest that the observed therapeutic enhancement was not broadly driven by canonical VEGF upregulation. Accordingly, we focused our subsequent mechanistic analyses on FGF2 signaling as a candidate mediator of the enhanced regenerative response. Having established the therapeutic efficacy of CN and CCN, we next assessed translational relevance using a gravity-driven cell aggregation method, which improves engraftment compared with single-cell delivery. Because aggregation inherently enhances cell retention, we reasoned that this approach would uncover additional benefits conferred by CN or CCN. Accordingly, CN or CCN were incorporated into the aggregation protocol, and subsequent experiments were performed.

Increased cell aggregation via enhanced cell settling speed with CN or CCN

CN or CCN-based cell aggregation methods improved the aggregation rate by increasing cell density and cell settling speed (**Fig. 4a**). Specifically, the initial cell aggregation rate was significantly accelerated when examined at 1 and 3 h after the cell aggregation (**Fig. 4b,c**). The aggregation rate was more than 20% faster in the CN or CCN groups compared to the NT group (**Fig. 4c**). Similar to 2D cell culture (**Fig. 3**), we found that CN or CCN enhanced the expression of adhesion-related genes and proteins during the cell aggregation (**Fig. 4d-f and Fig. S6a,b**). Notably, FGF2 protein, one of the key cytokines involved in the therapeutic pathway[35], expression was remarkably increased in the CCN groups at 1 and 3 h after the cell aggregation (**Fig. 4f**). Since FGF2 was consistently highly expressed only in the CCN groups, we hypothesized that Cu ions could affect the cellular mechanism. In addition, we found that cell density after cell aggregation consistently increased up to 24 h (**Fig. S6c**). We observed that after 24 h, the cell-settling NPs were distributed between the F-actin signals, confirming successful incorporation (**Fig. S6d**).

In vivo assessment of CCN-incorporated cell aggregation

To check the *in vivo* therapeutic effect of CN or CCN groups, we injected cell aggregates with or without NPs treatment into the skin wound mouse model and analyzed the wound tissues on day 14 after treatment (**Fig. 5a**). Although cell aggregates themselves have high cell retention, treatment with CN and CCN showed even higher therapeutic efficiency (**Fig. 5**). In particular, the analysis focused on the fact that CCN exhibited the highest therapeutic effect. From day 7 to 14 after the treatments, the CCN group showed significantly improved wound closing ratio compared to other groups (**Fig. 5b,c**). Also, FITC-positive involucrin and laminin signals were increased in the CCN group (**Fig. 5d**). Since involucrin and lamina layers are important for composing the skin layers, we concluded that the restoration of skin layers was also improved in the CCN group compared to other groups. In terms of vascularization, FITC-positive CD31 and α-SMA signals increased in the CCN group (**Fig. 5d**). The gene expressions from wound site tissues supported effective wound regeneration in the CCN group (**Fig. 5e**). After Mason's trichrome staining of wound regions, the percentage of collagen area was quantified (**Fig. 5g,h**). While all groups with cell injections decreased fibrosis during the wound healing process, the CCN group showed the lowest percentage of collagen regions in the wound region (**Fig. 5g,h**). Also, expressions related to fibrotic tissue, such as *Col1a1* and *Acta2*/*Pecam1* ratio, were significantly decreased in the CCN group (**Fig. 5f**). At the protein level, the Col3A1/Col1A1 ratio was increased in the CCN group (**Fig. 5i,j**), which is strongly associated with a reduction of fibrosis[36] . Although we increased the retention rate with CN or CCN even among aggregates, we conducted a detailed analysis of the mechanism, including protein analysis and RNA sequencing, to understand why CCN has the highest therapeutic efficiency.

Cellular mechanism study based on copper related protein analysis and RNA sequencing following CN or CCN incorporation

To elucidate the mechanism of FGF2 upregulation in CCN-treated cells, we first examined copper-associated regulators, focusing on copper chaperone–related genes. We then assessed copper-dependent signaling mediators, particularly those whose activity is known to be copper-sensitive. Based on these analyses, we directed our investigation toward the FGF2/MEK/ERK signaling axis and copper-responsive pathways (**Fig. 6**). Even after 24 h of cell culture, the amount of FGF2 secretion was significantly increased in the CCN group compared to other groups, which are consistent with the enhanced FGF2 secretion at 1 and 3 h (**Fig. 4d, Fig. 6a, and Fig. S7a**). Although copper ions are sometimes utilized by cells to improve the VEGF signaling pathway[37], there was no increase in HIF-1α and VEGF expression after CCN incorporation (**Fig. S7b,c**). Nonetheless, copper ions from CCN stimulated the expression of the copper chaperone, CCS, but not ATOX1, SOD1, and COX17 (**Fig. 6d, and Fig. S7c-e**). Therefore, we focused on the connection between CCS and FGF2 expression. In the FGF2/MEK/ERK signaling pathway, MEK and pMEK are activated by copper ions[38]. When we examined CCS, MEK, ERK, and FGF2 over 24 h (**Fig. 6b,c,e-h**), we found that they have strong relationships, especially in the protein expression of phosphorylated forms and FGF2. Besides, the upregulated FGF2 secretion also affected PCNA protein expression in the CCN group, which helps cell proliferation and rejuvenation (**Fig. 6b,c**) [39].

Although FGF2 is a well-known protein that induces MEK/ERK pathway activation[40], there was no proof that pERK can induce FGF2 expression through a positive feedback loop system. To confirm the FGF2 positive feedback loop mechanism, we utilized various inhibitors, including a CCS inhibitor (DC_AC50), an ERK inhibitor (U0126), and an FGF2 inhibitor (FGF2 antibody) (**Fig. 6a,f,g**). The CCS inhibitor decreased CCS and FGF2 gene expression levels (**Fig. 6g,h**). After CCS inhibition, there are no significant differences in CCS and FGF2 gene expression among the three groups (**Fig. 6g,h**). Both pERK/ERK and FGF2 expressions were reduced after treatment with the ERK inhibitor and FGF2 inhibitor (**Fig. 6f**). We confirmed that FGF2 follows a positive feedback loop mechanism and further verified the protein expression of FGF2 at 24 h through fluorescence staining (**Fig. 6i and Fig. S7f**). The enhanced anti-fibrotic effect and vascularization observed *in vivo* were supported by both FGF2 and biophysical effects such as increased cell density and adhesion induced by CN/CCN (**Fig. 5**). Therefore, we analyzed the direct effect of FGF2 on vascularization, fibrosis, migration, and other related processes.

We analyzed the effects of CN/CCN on cells and their underlying mechanisms through RNA sequencing **(Fig. 6)**. Although various genes showed up- or downregulation, several were particularly striking in their expression changes, suggesting a more pivotal role in the observed phenotype **(Fig. 6, Fig. S8-11)**. Our analysis confirmed copper ions and FGF2 were central to the activation of the ERK and MAPK pathways in the CCN group, consistent with the copper–ERK signaling relationship demonstrated in **Figure 6 (Fig. 7a)**. Cells treated with CN/CCN exhibited distinct alterations in gene expression compared to the NT group, with clear separation and differential expression patterns evident in the heatmap analysis **(Fig. 7b)**. The PCA plot revealed similarities in gene expression between the NT group and the CN/CCN-treated group **(Fig. S8b).** The NT and CN/CCN groups exhibited distinct differences in gene expression, and a clear separation was also observed between the CN and CCN groups. GO enrichment analyses for CN/NT and CCN/NT were aligned side-by-side using identical GO terms to enable direct comparative evaluation **(Fig. 7c)**. Regeneration-related GO terms, including positive regulation of angiogenesis and wound healing, were enriched in both treatment groups; however, distinct differences in enrichment magnitude were observed between CN/NT and CCN/NT in selected categories. Notably, differential enrichment was detected in GO terms related to detoxification of copper ions, cellular response to copper ions, copper ion transport, positive regulation of endothelial cell migration, and positive regulation of the ERK1 and ERK2 cascade **(Fig. 7d)**. These findings further support a mechanistic link between copper ion–associated processes and ERK pathway activation. Consistent with these enrichment patterns, key regulatory genes were significantly upregulated in the CCN-treated group. Notably, FGF2, a representative angiogenic growth factor, and several metallothionein genes (MT1X, MT1F, MT1G, MT1E, MT1M, and MT2A), which are involved in the transport and maintenance of copper ion homeostasis, were markedly increased compared with NT **(Fig. 7g, Table S1)**[41]. The coordinated upregulation of FGF2 and copper ion–associated metallothioneins further supports a functional coupling between copper handling and ERK-dependent angiogenic signaling. Through the DEG analysis, the GO of the CCN-treated group revealed various mechanisms that were highly activated by CCN in the cells **(Fig. 7c, Fig. S9)**. Notably, several GO terms related to copper ions, such as detoxification of copper ions, cellular response to copper ions, and copper ion transport, showed significant enrichment, suggesting a direct effect of copper ions on cellular functions. GO terms directly related to wound regeneration, including positive regulation of angiogenesis and wound healing, were also activated. Most of all, the upregulation of FGF2 played a pivotal role in the activation of all these GO terms.

Both CN and CCN treatments significantly enriched the GO term “cellular response to mechanical stimulus” **(Fig. 7c, Fig. S9)**, suggesting enhanced cellular adaptation to mechanical stress induced by particle uptake. This adaptation may contribute to improved cellular settling, retention, and increased local cell density. Hierarchical clustering heatmaps further demonstrated that, in the CCN vs NT comparison, MAP2K1 (MEK1) and FGF2 were significantly upregulated by 1.395-fold (adjusted p = 0.048) and 1.27-fold (adjusted p = 0.044), respectively, contributing to activation of the ERK1/2 cascade **(Fig. S8c)**. Similarly, genes associated with the positive regulation of angiogenesis, including HMOX1, ADM, and FGF2, were upregulated by 2.88-fold (adj p = 0.013), 1.28-fold (adj p = 0.032), and 1.27-fold (adj p = 0.044), respectively **(Fig. S8d)**. These genes are known to promote endothelial cell proliferation, migration, survival, and vascular stabilization, thereby facilitating vascular regeneration [42,43] . However, despite enrichment of the “cellular response to mechanical stimulus” term, canonical upstream regulators of cytoskeletal tension, stiffness, and mechanotransduction did not exhibit coordinated transcriptional activation **(Fig. S8e,f)**. Specifically, key mechanosensitive and contractility-associated regulators, including SRC, ROCK1/2, PIEZO 1/2, YAP1, TRPV4, and core RhoA signaling modules, remained transcriptionally unchanged following nanoparticle treatment **(Fig. S8e)**. Moreover, GO categories directly related to actin cytoskeleton organization, stress fiber formation, and cortical actin assembly did not demonstrate meaningful enrichment in either the CN/NT or CCN/NT comparisons **(Fig. S8f)**. No statistically significant enrichment was observed in regulation of actin cytoskeleton organization, actin cytoskeleton organization, stress fiber–associated categories, or cortical actin cytoskeleton organization in either the CN/NT or CCN/NT analyses. To further determine whether downstream mechanotransduction pathways were engaged, we examined canonical signaling modules associated with biomechanical force sensing. Coordinated activation of Hippo signaling or Rho protein signal transduction would be expected if nanoparticle-induced stiffening were the primary driver. In our results, while Hippo signaling was enriched in the CCN/NT comparison, it was not enriched in the CN/NT dataset **(Fig. S8f)**. The absence of consistent activation across both nanoparticle conditions suggests that this enrichment is unlikely to reflect a direct physical stiffening effect of nanoparticle embedding. Moreover, Rho protein signal transduction was not enriched in either comparison.

KEGG pathway analysis was performed by directly comparing CN/NT and CCN/NT across matched pathway categories **(Fig. 7e, Fig. S10)**. The mTOR signaling pathway, PI3K-Akt signaling pathway, Rap1 signaling pathway, and MAPK signaling pathway exhibited greater activation in the CCN group compared with CN **(Fig. 7f)**. Notably, these four pathways all include FGF2 as an upstream regulatory component, and differential activation between CN and CCN was consistently observed across these FGF2-associated pathways. Although oxidative phosphorylation was also enriched, this increase was interpreted as a metabolic adaptation associated with CN/CCN particle uptake rather than a primary mechanistic driver. DEG-based KEGG analysis of the CCN group further revealed enrichment of protein synthesis–related pathways, including protein processing in the endoplasmic reticulum, spliceosome, and ribosome pathways **(Fig. 7g, Fig. S10)**. MAPK-associated pathways, including the mTOR signaling pathway and phospholipase D signaling pathway, were also activated. FGF2 and MAPK were linked to activation of the PI3K-Akt, Rap1, and MAPK signaling pathways. Among these pathways, the mTOR, Rap1, and MAPK signaling pathways exhibited a significantly greater number of upregulated genes than downregulated in the CCN group, whereas the PI3K-Akt pathway showed a modest predominance of upregulated genes. In contrast, only the mTOR signaling pathway was activated in the CN group, and its fold enrichment was lower than that observed in CCN **(Fig. S7c)**. We subsequently investigated these signaling alterations under in vitro conditions. We proceeded to analyze the signaling pathways and their alterations under *in vitro* conditions.

We harvested concentrated culture media from each group as shown in **Figure 8a**. In the wound scratch assay, the CCN group demonstrated a significantly enhanced migration rate compared to other groups (**Fig. 8b,c**). Cytokine array analysis revealed that migration-related cytokines, including CXCL1, CXCL10, IL-6, IL-8, and G-CSF, were elevated in the CCN group compared to other groups (**Fig. S11a**). Correspondingly, migration- and proliferation-associated genes, CXCR4, MKI67, and PCNA, were upregulated in the CCN group compared to other groups (**Fig. 8d and Fig. S11b**). Furthermore, inflammation-related cytokines were altered following treatment with cell-settling nanoparticles. In contrast, CN and CCN had minimal effects on THP-1 cell differentiation, suggesting that they exert limited influence on the inflammatory cell differentiation process (**Fig. S11c**).

Given the strong association of FGF2 with fibrosis and myofibroblast differentiation, we treated myofibroblasts with inducible TGF-β and CM derived from each group (**Fig. 8e,f**). Both CN and CCN inhibited myofibroblast differentiation via FGF2 signaling, which correlated with the levels of FGF2 protein expression (**Figs. 6, 7, 8e, and S6a**). The FGF2 expression was markedly higher in the CCN group. The CCN group exhibited the most significant *in vivo* therapeutic effect, whereas CN showed minimal differences compared to the NT group (**Fig. 5**). To further clarify these anti-fibrotic effects, we analyzed additional genes and proteins to evaluate the anti-fibrotic potential of CCN (**Fig. 8e and Fig. S11a**). Notably, fibrosis-inducible factors such as NF-κB, α-SMA, WNT, COL1A1, and TGF-β were substantially reduced in the CCN CM-treated group compared to other groups (**Fig. 8f**). FGF2, abundantly secreted only by the CCN group, significantly enhanced endothelial tube formation, leading to a marked increase in node and mesh formation **(Fig. 8g,h**). These findings led us to conclude that cytokine modulation through CCN aggregates significantly improves therapeutic outcomes. Enhanced cell adhesion and increased local density were important contributing factors to the superior retention and wound healing efficacy, alongside the key role of FGF2 upregulation induced by CCN.

Discussion

Physical forces such as gravity and resistive forces, mediated by our one-pot synthesized biocompatible CN and CCN nanoparticles, contributed to enhanced intercellular incorporation, cell density, and adhesive interactions without compromising cell viability or proliferation. Notably, CN and CCN differentially upregulated key adhesion markers in both 2D and 3D cultures, with CCN further promoting the expression linked to FGF2 signaling and improved regenerative outcomes. Physical forces such as gravity and buoyant forces not only shape tissue architecture but also influence key biological processes, including cell adhesion and tissue regeneration. Despite its importance, the therapeutic potential of this approach has remained underexplored. In this study, we developed biocompatible CN and CCN synthesized via one-pot synthesis to achieve effective intercellular incorporation. We found that gravitational settling mediated by CN or CCN significantly increased cell density, thereby enhancing adhesive interaction. Following CN or CCN treatment, the expression of various adhesion-related markers, such as CD44, Cx43, and N-cadherin, increased. The CD44 proteins form a ubiquitously expressed family of cell surface adhesion molecules involved in cell-cell and cell-tissue adhesion[44]. In the 2D cell culture condition, only CN increased CD44 expression, whereas both CN and CCN induced upregulation in 3D conditions. Although the increased CD44 in MSCs has improved migration[45], we observed no significant difference in migration between CN and CCN groups in 2D culture (**Fig. S12**). Importantly, increased cell density did not negatively impact mitosis or proliferation. These results were also observed in cell aggregates, where the formation of spheroidal structures was confirmed without any noticeable issues. As FGF2 induced the upregulation of a panel of mesenchymal N-cadherin and phosphorylates cardiac Cx43 at sites of intercellular contact[46,47], CCN improved N-cadherin and Cx43 expression. In contrast, integrin α5, which primarily mediates cell–substrate adhesion, showed no difference among NT, CN, and CCN groups, indicating that its expression is less influenced by cell–cell aggregation[48]. Following aggregation, we observed a marked increase in low-molecular-weight FGF2, which correlated with enhanced wound healing and reduced fibrosis in all cell-injected groups[49].

Building on our exploration of nanoparticle-driven cell adhesion and the novel FGF2–ERK positive feedback loop, we demonstrate that advanced nanoparticle design (from CN to CCN) not only markedly enhances cellular retention, vascularization, and anti-fibrotic wound healing but also unveils previously unrecognized, self-sustaining signaling circuits with broad therapeutic potential. First, we elucidate the relationship between cell adhesion and physical forces. We have redefined the directionality of conventional nanoparticles and introduced the concept of regulating cell density. This cell-settling process has potential applications across various fields, including therapeutics, cell biology, and developmental studies. Secondly, we investigated the FGF2 positive feedback loop system. While the downstream effects of FGF2/FGFR are well known, there has been no evidence that pERK/ERK can induce FGF2 through a positive feedback loop. RNA sequencing results also supported that the process subsequently triggered the FGF2/FGFR signaling pathway, creating a positive feedback loop. This suggests that the activation of downstream pathways of MAPK signaling, such as the PI3K-Akt signaling pathway and the Rap1 signaling pathway, serves as evidence of the positive feedback loop. Notably, FGF2 played a critical role in all of these activations as well. Utilizing signaling inhibitors, we demonstrated this mechanism, providing deeper insights into the FGF2 signaling pathway. Our findings indicate a previously underexplored FGF2–ERK positive feedback loop, which may serve as a self-sustaining signaling circuit to maintain regenerative signaling even after initial CCN-mediated priming. Finally, we established that the cell-settling process can be harnessed for therapeutic purposes. The development from CN to CCN significantly enhanced cell retention, vascularization, and anti-fibrotic wound healing. With surface modification, CN holds great promise for targeting various diseases. Beyond its immediate biomedical relevance, this study underscores the importance of a biophysical approach in advancing cell-based therapies. To our knowledge, there are limited prior studies that specifically employ nanoparticle-mediated density tuning to enhance gravity-driven cell settling as a strategy to improve local retention, which makes direct one-to-one comparison challenging. Recent studies demonstrated therapeutic benefits following nanoparticle internalization[50–52] , they largely focus on biochemical or molecular effects and rarely evaluate the impact of nanoparticles on cellular physical properties such as density or sedimentation behavior. In our study, by introducing density modulation as a new principle of control, the paradigm of cell regulation is extended beyond biochemical strategies to include physical forces. In doing so, our approach extends nanoparticles beyond their conventional role as biochemical carriers, positioning them as physical modulators of cell behavior through density tuning. Such a framework can be applied to the design of scaffolds, hydrogels, and nanoparticles, where density tuning may provide a powerful lever to engineer cell–material interactions and collective behaviors. In biotechnology, it provides a versatile and safe means of enhancing stem cell engraftment, modulating organoids, and optimizing bioprinting architecture. At the translational level, this concept lends itself to scalable manufacturing and quality control, reducing costs associated with poor engraftment while broadening patient accessibility. More broadly, emphasizing physical regulation in biology opens a path for rethinking how mechanical and material properties shape cellular function and provides a conceptual foundation for training the next generation of researchers at the intersection of physics, engineering, and medicine. For further study, it would be highly beneficial to conduct an analysis to cover the incorporation process of CN into cells and modify the surface to achieve rapid incorporation and give specific cellular mechanism activation.

While our approach shows significant promise, several limitations warrant discussion and suggest directions for future research. First, cell populations may exhibit heterogeneous uptake of CN and CCN, which could lead to diverse mechanical and biochemical responses among subpopulations. Because our measurements were performed at the bulk population level, we did not explicitly resolve cell-to-cell variability in nanoparticle uptake. Therefore, it is possible that a subset of cells incorporated fewer CN/CCN and consequently experienced a reduced effect. Moving forward, detailed single-cell analyses will be crucial for gaining a more precise understanding of cellular responses to nanoparticle exposure, thereby enhancing the resolution and utility of our findings. Second, we hypothesized that nanoparticle surface charges (specifically, zeta potential) may influence cell adhesion and, consequently, intracellular accumulation. To mitigate confounding effects from surface charge variability, we standardized our experiments using nanoparticles with a zeta potential of –25 mV. However, these findings suggest an opportunity for further optimization: future work could systematically investigate the impact of more positively charged nanoparticle surfaces, which may enhance both cellular adhesion and intracellular accumulation through increased weight-driven sedimentation. Such refinements would provide valuable mechanistic insights and could further improve the efficacy of nanoparticle applications in this context. Third, in our bulk analyses, key morphological parameters, including major and minor axis lengths and cellular eccentricity, did not show substantial changes before and after nanoparticle treatment. While these observations suggest that gross cell shape was largely preserved, we acknowledge that modeling cells as perfectly rigid spheres represents a conceptual simplification. This idealized Stokes-based framework does not fully capture the contributions of active cell motility, cell–cell interactions, or subtle shape dynamics inherent to living cells, and therefore we cannot fully rule out the possibility that biophysical changes — such as alterations in cell motility or stiffness — may have contributed to the observed outcomes as an additional, complementary component of the overall mechanism. That said, in our settling assays, cells settled rapidly, typically within approximately 1 minute under gravitational force. Over this short timescale, passive settling forces are expected to dominate over active motility or dynamic intercellular interactions, suggesting that gravity-driven sedimentation was the primary driver in our experimental context. Nevertheless, we recognize that these biological factors may become increasingly influential over longer durations or under different mechanical contexts, and future studies incorporating single-cell biophysical measurements would help clarify their relative contributions. While the simplified physical model provides conceptual insight into relative settling behavior, it does not account for all biophysical complexities of living cells. Fourth, we also acknowledge that in vivo cell behavior is influenced by multiple physical forces, including shear stress, tissue motion, and intrinsic cell motility. However, the relative contribution of these forces is context dependent. In this study, we employed a dorsal skin wound model in mice that represents a relatively static cutaneous injury environment with limited imposed flow or mechanical disturbance[53] . We recognize that the directionality of the gravitational vector is an important consideration in the context of cell settling and retention. Importantly, however, in both mice and humans, the gravitational vector relative to any given wound site is not fixed — it naturally varies with body posture, movement, and anatomical orientation over time. Despite this inherent variability, we confirmed through our in vivo wound healing outcomes and the adhesion kinetics that CN/CCN-incorporated cells maintain robust and prolonged retention at the target site. We attribute this to the rapid establishment of initial adhesive contacts within approximately 1 minute of settling, after which cells sustain attachment through upregulated adhesion molecule expression — including CD44, N-cadherin, and Cx43 — that persists independent of gravitational directionality. These findings suggest that once initial adhesion is established, long-term retention and therapeutic efficacy are maintained even as the gravitational vector changes with normal movement, supporting the potential applicability of this platform across diverse wound environments and tissue sites. We therefore believe that the natural variability of gravitational vectors in living subjects does not fundamentally limit the translational potential of this approach. In clinical settings, body positioning during and immediately after cell administration could be used to leverage gravitational force in a targeted manner, similar to positioning strategies already employed in intrathecal or intra-articular drug delivery protocols[54]. We also acknowledge that the mouse dorsal wound model represents a simplified preclinical system, and that larger animal studies — such as porcine models, which bear well-documented anatomical and physiological similarities to humans — with more anatomically complex wound sites will be necessary to fully validate the translational relevance of this approach in humans. Although centrifugation is commonly used to promote cell aggregation, the gravity imposed by centrifugal force can itself modulate cellular signaling in a force-dependent manner, and the directionality as well as long-term biological consequences of such modulation remain incompletely understood[15,55]. Importantly, for nanoparticle-integrated cells, the use of high centrifugal forces raises additional concerns. Excessive centrifugation may drive aberrant nanoparticle penetration into intracellular compartments, potentially altering organelle integrity, cellular signaling, and cytotoxicity in unpredictable ways. In conventional protocol, stable co-assembly of cells with nanoparticles required centrifugal forces approaching ~8,000 rpm, a regime that is likely to impose substantial mechanical stress and compromise cell viability. These considerations highlight the importance of developing assembly strategies that leverage physiologically relevant forces rather than relying on extreme mechanical compaction. In this regard, our density-modulation strategy using nanoparticle-integrated cells represents an improvement by enabling controlled sedimentation without exposing cells to excessive centrifugal stress. Nevertheless, alternative aggregation and assembly approaches should be further explored and systematically compared to optimize cellular integrity, mechanotransduction stability, and long-term therapeutic performance. Fifth, it should also be noted that intravenous (IV) delivery warrants careful consideration in the context of this platform. In an intravascular environment, blood flow-induced shear stress dominates over gravity-driven sedimentation, and the density increase conferred by CN/CCN may promote premature sedimentation before cells reach the target site, raising concerns regarding reduced therapeutic efficacy and potential vascular occlusion. Indeed, prior studies have documented that IV-injected MSCs are predominantly trapped within pulmonary microcirculation in the early post-injection period[56] . These considerations suggest that if IV delivery were to be explored in future studies, additional engineering strategies — such as surface modifications to reduce density-dependent sedimentation under flow conditions — would need to be developed and validated to ensure both safety and therapeutic efficacy. We therefore consider the current platform most suited to local or minimally invasive delivery routes, such as intradermal, subcutaneous, intra-articular, or direct wound-site injection, where gravitational forces can be transiently harnessed to improve initial cell retention, while acknowledging that extension to systemic delivery routes remains an important and open direction for future investigation. At the same time, nanoparticle-based approaches will still require thorough safety and regulatory evaluation prior to clinical translation. Copper-containing formulations are under clinical investigation (e.g., NCT04167969). MSC-based therapies have been approved in South Korea, and certain silica-based nanoparticle platforms have received regulatory authorization for intravenous administration in the United States[57,58]. Although the use of clinically familiar materials, such as silica-based nanoparticles and trace amounts of copper, may simplify regulatory considerations relative to gene-based therapies, it does not eliminate the need for rigorous preclinical and clinical safety assessment.

In summary, this study provided evidence for the proportional effect of gravity on cell adhesion efficiency through the cell uptake of copper ion-releasing nanoparticles. Further design enhancements were able to enhance the therapeutic efficacy of 3D cell spheroids. Controlling physical forces could be a solution for reducing side effects and maintaining long-term safety in cell-based biomedical engineering. We anticipate that this cell settling system will open new avenues for cell therapy and serve as a foundation for diverse biophysical research.

Methods

CN and CCN synthesis

CCN was prepared by coating copper particles with CN through a one-pot synthesis. 10.5 g of Brij-C10 (Polyethylene glycol hexadecyl ether, average molecular weight ~ 683, Sigma-Aldrich, St Louis, MO, USA) was dissolved in 50 mL of cyclohexane (Cyclohexane, 99.5%, Samchun Chemical, Seoul, Korea) at 50 °C, 700 rpm overnight. Then, $Cu(NO_3)_2 \cdot 3H_2O$ (Copper(II) nitrate trihydrate, 99.0%, Daejung Chemicals, Siheung, Korea) was dissolved in DI water to create a 0.15 M solution. When all of the Brij-C10 is dissolved, 1.5 mL of DI water or Cu solution (0.15 M) was added. After 1 h, 3 mL of ammonia water (NH_4OH, 25 ~ 30%, Deoksan, Ansan, Korea) was added to the mixture drop by drop using syringe pump. After 2 min, 5 mL of tetraethyl orthosilicate (TEOS, 98.5%, Daejung Chemicals) was added dropwise, and the temperature was maintained at 50 °C at 700 rpm for 2 h. Three rounds of centrifugation were done at a speed of 8,000 rpm for 10 min with EtOH. The collected solid powder was dried overnight at 80 °C in a convection oven and then calcined for 2 h at 550 °C with 1 °C/min ramping rate in an air atmosphere to eliminate residual organics and strengthen the mechanical properties of the CN shell. CN consists of a silica core, whereas CCN is composed of the same silica core with copper localized on the particle surface. For making rhodamine-CN, the rhodamine-APTES conjugate was co-condensed with TEOS to prepare the silica network before EtOH washing[57].

X-ray diffraction (XRD) and X-ray fluorescence (XRF)

Small-angle and wide-angle powder XRD of the fresh and used supported NP catalysts were analyzed to verify ordered mesoporous structure of the specific supports and the crystalline phases and sizes of CN or CCN before and after the DRM reaction using a X' Pert PRO MPD (PANalytical, Almelo, Netherlands) instrument operated with a Cu-K α radiation of 0.15406 nm at maximum 60 kV and 55 Ma. For the small-angle X-ray scattering analysis, the collected scattering vector (q, nm^{-1}) was converted to a two theta value using the equation $q = 4\pi \sin(\times / \lambda)$, where λ is the Cu-K α radiation of 0.15406 nm. For the wide-angle XRD, the samples were scanned in a range of 5 – 90 ° with a rate of 5/min. The full width at half maximum values of the deconvoluted main CN or CCN diffraction peak at a Bragg angle of $2 \times = 23.3$ ° were used for the calculations of their average crystallite sizes by the Scherrer equation, using a Scherrer constant of 0.9, assuming that crystallites are in a spherical shape. XRF analysis by using an S8 Tiger (Bruker, MA, USA) instrument operated at 60 kVm and 50–170 mA was used to verify the bulk Si/Cu ratio of CN and CCN.

TEM

The surface morphologies and CN and CCN size distributions on the fresh and used supported NP catalysts were characterized by TEM using a JEM-2100F instrument operating at 200 kV. Spatially confined NPs in the mesoporous channels on the selected fresh and used NP(10)/SBA-15 were visualized by means of scanning transmission electron microscopy bright field image (STEM-BF) in the same equipment.

Cell culture

All experiments involving human-derived cells were conducted in accordance with relevant guidelines and regulations and complied with the principles outlined in the ISSCR Guidelines for Stem Cell Research and Clinical Translation. MSCs were purchased from Lonza (Walkersville, MD, USA). The MSCs used in this study were adipose-derived MSCs (Cat. No. PT-5006). Prior to use, their identity and basic characteristics were validated according to the manufacturer's data sheet, including the expression of standard MSC surface markers. The cells were cultured in cell culture dishes (Corning, Steuben, NY, USA) with Dulbecco's modified Eagle's medium (Gibco BRL, Gaithersburg, MD, USA) supplemented with 10% (v/v) fetal bovine serum (FBS; Gibco BRL) and 1% (v/v) penicillin–streptomycin (PS; Gibco BRL), in a 37 °C cell incubator at 5% CO_2 conditions. The culture medium was changed every 2 days, and the MSCs in passages 5–7 were used in subsequent experiments. The MSCs used in this study were obtained from commercial sources and used according to the supplier's documentation and characterization data. All cell lines were confirmed to be negative for mycoplasma contamination. The cell lines were also checked against the ICLAC database, and no known misidentified or cross-contaminated cell lines were used in this study.

CN or CCN were introduced directly into the MSC culture medium, allowing the cells to internalize or associate with the nanoparticles under standard culture conditions. For experiments involving aggregation, including the hanging drop method, nanoparticles were added to the hanging drop medium and co-cultured with MSCs during aggregate formation.

Individual cell density

CN-internalized cell density was calculated by dividing the total single-cell weight by the measured cell volume. Total single-cell weight was defined as the sum of the intrinsic cellular mass (cell density × cell volume) and the additional mass contributed by internalized CN or CCN. Nanoparticle-derived mass per cell was quantified using two independent approaches **(Fig. S13)**: fluorescence-based calibration and dry mass measurement. Fluorescence intensity was converted to nanoparticle mass (μg per cell) using a standard calibration curve within the validated working range. In parallel, dry mass measurements were independently performed to estimate total cellular mass. Comparison of the two methods revealed no significant difference between fluorescence- and dry mass-derived cell density. Based on this consistency, both measurements were incorporated to estimate total single-cell weight and calculate the adjusted cell density.

Computational and theoretical modeling of cell sedimentation

The sedimentation of cells in a viscous medium was modeled using a commercially available finite element analysis software. For each of the three conditions, the fluid-filled domain was modeled with spatial dimensions of 4 cm by 8 cm. The fluid was modeled with a density of 1.007 g/mL and a viscosity of 0.001 Pa·s. The viscosity of the liquid was adjusted to facilitate effective monitoring of the cell's displacement. Three cells were released at a height of 7 cm from the bottom of the domain. Each cell had a diameter of 30 μm and a density of 1.0525, 1.4208, or 2.1855 g/mL, corresponding to one of the three conditions. Gravitational and buoyant forces were applied to the cells, using the previously defined fluid density and viscosity. The linear Stokes regime was used for the drag coefficient. Cell motion was governed by Newton's Second Law, incorporating gravitational and resistive forces. The governing equation can be expressed as:

$$(1)\ m\frac{d\mathbf{v}}{dt} = -6\pi\eta r(\mathbf{v}-\mathbf{u}) + mg - \mathrm{V}\rho_f g$$

where m is the cell mass ($m = \rho_c V$), $\mathbf{v}$ and $\mathbf{u}$ are the cell and fluid velocities, respectively, g is the gravitational acceleration, r is the cell radius, ρ_c and ρ_f are the cell and fluid densities, V is the cell volume, and η is the fluid dynamic viscosity. The fluid velocity $\mathbf{u}$ is equal to zero. The drag force was calculated based on Stokes' law, which is valid under low Reynolds number conditions ($Re \ll 1$). Theoretical study was calculated using the following equation based on Stokes' law:

$$(2)\ d(x) = \frac{2}{9}\cdot\frac{(\rho_c-\rho_f)gr^2}{\eta}\cdot t$$

where $d(x)$ is the cell displacement, t is the duration time, and all other terms are as previously defined. The reasoning for approximating the motion of the particle using the terminal velocity assumption is provided in the Supplementary Information.

F-actin staining (phalloidin)

F-actin staining was performed to visualize adherent cells and to quantify the number of MSCs attached to the plate following CN or CCN treatment. The MSCs cultured on a 6-well plate with nanoparticles were fixed with 4% paraformaldehyde (Biosesang, Sungnam, Korea) for 10 min, then washed with PBS. After washing twice, cells were stained with TRITC-phalloidin, which contained a mounting medium (VECTASHIELD H-1600; Vector, Burlingame, CA, USA), and at the same time counterstained with 4,6-diamidino-2-phenylindole (DAPI, Vector Laboratories, Newark, CA, USA).

Cryo-TEM

Cryogenic transmission electron microscopy (Cryo-TEM) was performed to evaluate the intracellular retention of CN or CCN nanoparticles over time. CN- or CCN-treated MSCs were vitrified and subjected to cryo-focused ion beam (cryo-FIB) milling to generate thin cellular cross-sections suitable for transmission electron imaging. Lamellae were prepared using an Aquilos 2 Cryo-FIB (Thermo Fisher Scientific, Waltham, MA, USA). Cryo-TEM images were acquired using a Glacios Cryo-TEM (Thermo Fisher Scientific) operated at an accelerating voltage of 200 kV. Data was collected using EPU software (Thermo Fisher Scientific).

CN/CCN coated PDMS fabrication and contact angle

To fabricate polydimethylsiloxane (PDMS, Sylgard 184) gel containing particles, we prepared 1 g of 10 wt% PDMS prepolymer. Then, two types of particles (CN and CCN) were added to each PDMS prepolymer at different concentrations (0 or 20 mg) and mixed well for 1 min. These mixtures containing CN or CCN were placed in 100 μL each in a 96-well plate and cured in an oven at 80 °C for 2 h. Contact angle was measured by dropping deionized water onto PDMS substrates with and without CN or CCN.

MSC spheroid culture

MSC spheroids were cultured following the hanging drop method[58]. The cell drops (3×10^4 cells/drop) with 25 μL of cell culture medium were incubated hanging under the lid of a petri dish for 24 h to form MSC spheroids. In the case of using nanoparticles, each of them was added to the spheroid culture medium at a concentration of 400 μg/mL.

Flow cytometry

The surface staining of cells was performed using fluorescent DiI staining, which overlaps with PE in excitation, for the PE-NT group. Additionally, SSC analysis was conducted to check the cells after CN or CCN incorporation. The cells were washed with 500 μL of FACS buffer (1% FBS in PBS) and centrifuged at 350 x g for 2 min. Cell strainers were used to obtain a single-cell suspension in FACS buffer. The cells were then analyzed using a MACSQuant® VYB (Miltenyi Biotec). Data was analyzed with FlowJo software.

For sedimentation analysis, non-treated (NT) MSCs were first labeled with PE and mixed with CN-treated MSCs at an initial 1:1 cell ratio. The mixed cell suspension was gently layered into the upper phase of the same culture medium without agitation and allowed to settle under gravity for 1 min at room temperature, in the absence of any external force. After the settling period, the supernatant fraction was carefully collected from the top using a burette to avoid disturbing settled cells. Prior to flow cytometric analysis, the collected cells were gently resuspended and sufficiently dispersed to obtain a single-cell suspension, and FACS measurements were performed immediately to minimize re-settling effects. The relative proportions of PE-labeled NT cells and CN-treated cells remaining in the suspended fraction were quantified based on fluorescence signals.

qRT-PCR

qRT-PCR was used to analyze the relative expression levels of various genes (human GAPDH, CD44, N-cadherin, Integrin α5, Cx43, CCS, ERK, FGF2, PCNA, CXCR4, MKI67, CD80, CD163, CD206, TNF- α, IL-1β, TGF-β, NF-kB, WNT, Col1A1, HIF-1α, α-SMA, CD90, CD105, and mouse *β-actin*, *Fgf2*, *Mki67*, *Vegf*, *Ivl*, *Acta2*, *Pecam1*). Primer sequences were designed using Primer-BLAST (NCBI). Total ribonucleic acid (RNA) of each sample was isolated by using 1 mL Trizol reagent (Life Technologies, Inc, Carlsbad, CA, USA) and 200 µL chloroform. The samples extracted were centrifuged at 12,000 x g for 10 min at 4 °C. The RNA pellets were washed with 75% (v/v) ethanol in water, dried and dissolved in RNase-free water. To synthesize complementary DNA, reverse transcription was performed with 1.5 µg pure total RNA and the Primescript RT Master Mix (Takara, Kusatsu, Shiga, Japan). For qRT-PCR analysis, a cDNA solution, primers (obtained using Primer-BLAST), and SsoAdvancedTM Universal SYBR Green Supermix (Bio-Rad, Hercules, CA, USA) mixture were analyzed using the CFX ConnectTM real-time PCR detection system (Bio-Rad).

RNA sequencing

RNA sequencing (RNA-seq) was performed to investigate mechanistic changes at the RNA level in MSCs following CN or CCN treatment. Total RNA was extracted as described in the qRT-PCR section and dissolved in RNase-free water. RNA quality was assessed by measuring RNA concentration and integrity prior to library preparation. The cDNA library was generated using the CORALL RNA-Seq V2 Library Prep Kit (Lexogen, Vienna, Austria), and high-throughput sequencing was performed as paired-end 100 bp reads on a NovaSeq 6000 platform (Illumina, San Diego, CA, USA) with four biological replicates per group (n = 4). Raw sequencing data were quality-checked using FastQC and processed with Fastp for adapter trimming and removal of low-quality reads. Trimmed reads were aligned to the reference genome using STAR, and transcript quantification was performed using Salmon. Differentially expressed genes (DEGs) were identified using thresholds of fold change > 1.25 and P < 0.05. Selected DEGs were used for heatmap visualization, principal component analysis (PCA), gene ontology (GO), and Kyoto Encyclopedia of Genes and Genomes (KEGG) pathway analysis.

Western blot

Western blot analysis was performed to assess relative protein expression levels in various cell and tissue samples. MSCs and mouse tissue samples were lysed in radioimmunoprecipitation assay (RIPA) lysis buffer (Rockland Immunochemicals Inc., Limerick, PA, USA). The phosphate form of proteins was observed by resuspending the EDTA (Sigma-Aldrich) and phosphatase inhibitor cocktail in lysis buffer. The protein extracts were obtained after 2 h of shaking and centrifugation at 10,000 x g for 10 min, then the supernatant was collected. The protein concentrations were measured using a bicinchoninic acid (BCA) protein assay kit (Pierce Biotechnology, Rockford, IL, USA). Then, sodium dodecyl sulfate polyacrylamide gel electrophoresis (SDS-PAGE) was performed using 10% resolving gels with an equal amount of protein from each sample mixed with the sample buffer. After the proteins were separated, they were transferred to polyvinylidene fluoride membranes (Bio-Rad) and probed overnight with anti-GAPDH (ab9485, Abcam), anti-CD44 (ab189524, Abcam), anti-N-cadherin (ab18203, Abcam), anti-Integrin α5 (ab179475, Abcam), anti-Cx43 (ab235585, Abcam), anti-CCS (22802-1-AP, Proteintech, Rosemont, IL, USA), anti-pMEK (CS8727, Cell Signaling Technology, Danvers, MA, USA), anti-MEK (CS9154, Cell

Signaling Technology), anti-pERK (CS9101, Cell Signaling Technology), anti-ERK (CS9102, Cell Signaling Technology), anti-FGF2 (ab208687, Abcam), anti-VEGF (ab46154, Abcam) anti-β-Actin (ab213262, Abcam), anti-PCNA (ab18197, Abcam), anti-Col1A1 (ab34710, Abcam), and anti-Col3A1 (A0817, Abclonal, Wuhan, China)antibodies at 4 °C. Then, membranes were rinsed three times and incubated with horseradish peroxidase-conjugated secondary antibody (R&D Systems) at room temperature for 1 h. The blots were produced on luminescence recording X-ray film (Agfa HealthCare NV, Mortsel, Belgium) and imaged with Photoshop CC (Adobe Systems). Primary antibodies were used at the following dilutions: anti-GAPDH (1:5,000), anti-CD44 (1:1,000), anti-N-cadherin (1:1,000), anti-Integrin α5 (1:1,000), anti-Cx43 (1:1,000), anti-CCS (1:1,000), anti-pMEK (1:1,000), anti-MEK (1:1,000), anti-pERK (1:1,000), anti-ERK (1:1,000), anti-FGF2 (1:1,000), anti-VEGF (1:1,000), anti-β-Actin (1:5,000), anti-PCNA (1:1,000), anti-Col1A1 (1:1,000), and anti-Col3A1 (1:1,000). Horseradish peroxidase-conjugated secondary antibodies were used at 1:3,000.

Immunochemistry staining

Immunocytochemical staining was performed to visualize intracellular protein expression of target proteins. The MSCs spheroids were fixed with 4% paraformaldehyde (Biosesang) at room temperature for 10 min. Using a microscope (CKX53; Olympus, Tokyo, Japan), the morphology of the spheroid was analyzed. The fixed spheroids were embedded in a compound with optimal cutting temperature (O.C.T. compound, Scigen Scientific, Gardena, CA, USA). The samples were then frozen and sectioned at −20 °C into 10-μm sections. These spheroid sections were stained immunocytochemically to visualize FGF2 (ab208687, Abcam), CCS (22802-1-AP), F4/80 (ab300421, Abcam) with fluorescein isothiocyanate (FITC)-conjugated secondary antibodies (Jackson ImmunoResearch Laboratories, West Grove, PA, USA). In addition, these sections were also stained with DAPI and TRITC-phalloidin, which contained a mounting medium (VECTASHIELD H-1600; Vector, Burlingame, CA, USA) to stain nuclei and F-actin of MSCs. All section samples were observed under a fluorescence microscope (DFC 3000G; Leica, Wetzlar, Germany). Primary antibodies against FGF2, CCS, and F4/80 were used at dilutions of 1:100, 1:100, and 1:200, respectively. Fluorophore-conjugated secondary antibodies were used at 1:200. TRITC-phalloidin was used at 1:100, and nuclei were stained with DAPI-containing mounting medium.

Human cytokine array

The expression of immunomodulatory cytokines in spheroid CM was examined using the Proteome Profiler Human Cytokine Array Kit (R&D Systems, Minneapolis, MN, USA) in accordance with the manufacturer's instructions. The pixel density in each location was measured using ImageJ software (National Institutes of Health, Bethesda, MD, USA), and the average signal for the duplicate spots was calculated.

ELISA

The amounts of growth factors in the CM obtained from MSC spheroids were measured using ELISA kits for human FGF2 (R&D Systems) and VEGF (R&D Systems) according to the manufacturer's protocol to evaluate their paracrine secretion levels.

THP-1 cell culture and differentiation

THP-1 cells were used to evaluate the immunomodulatory effects of CM derived from experimental groups. THP-1 cells were purchased from American Type Culture Collection (ATCC, Manassas, VA, USA; Cat. No. TIB-202) and cultured in cell culture flasks (Corning) with RPMI-1640 medium (11875, Gibco BRL), supplemented with 10% (v/v) FBS (Gibco BRL) and 1% (v/v) PS (Gibco BRL), in a 37 °C cell incubator at 5% CO_2 conditions. The cell culture medium was replaced every second day, and THP-1 cells at passages 2–5 were used in the experiments. THP-1 cells were treated with 100 nM of phorbol 12-myristate 13-acetate (PMA, Sigma-Aldrich) for differentiation[59]. Then, cells were washed with PBS and incubated with MSC spheroid CM for 2 days to polarize toward the M1 or M2 phenotype.

HUVEC tube formation assay

The tube formation assay was performed to evaluate the pro-angiogenic potential of CM obtained from each experimental group. The tube formation assay was conducted with HUVECs using an Angiogenesis assay kit (ab204276, Abcam) according to the manufacturer's protocols. HUVECs were purchased from PromoCell (Heidelberg, Germany; Cat. No. C-12203). HUVECs were cultured with MSCs spheroid CM on pre-coated Matrigel (Corning)[60].

Migration assay

The migration assay was performed to assess the effect of CM on fibroblast migration. The migration assay was conducted using confluent human dermal fibroblasts (hDFs; PromoCell; Cat. No. C-12300) in a 6-well plate. The scratch wound of hDF was made using a 1,000 μL pipette tip and cocultured with the MSCs spheroid immediately. For every condition, the scratch size was measured after 24 h[61].

Mouse wound healing model

All animal experiments were performed in accordance with relevant guidelines and regulations and were approved by the Institutional Animal Care and Use Committee (IACUC) of Sungkyunkwan University (SKKUIACUC2023-10-19-1). Mice were housed under specific pathogen-free conditions with a 12 h light/12 h dark cycle, at an ambient temperature of 22 ± 2 °C and relative humidity of 50 ± 10%, with free access to food and water. 6-week-old female athymic mice (BALB/c nu/nu, 20–25 g body weight, Orient Bio Inc., Sungnam, Korea) were anesthetized with 200 μL xylazine (10 mg/kg) and ketamine (100 mg/kg) diluted in standard saline solution. During surgery and throughout the immediate recovery period until full awakening from anesthesia, animals were placed on a heated pad to prevent hypothermia and reduce procedural stress. Each mid-dorsal skin region of the mouse was sliced to create a full-thickness skin wound (2.0×2.0 cm^2)[62]. Then, each of experimental groups were randomly assigned to mice that had skin wounds (n = 6 per group: NT; NT SP treated group (6×10^5 cells suspended in 200 μL per mouse); CN SP treated group (6×10^5 cells suspended in 200 μL per mouse); CCN SP treated group (6×10^5 cells suspended in 200 μL per mouse)) The control group was NT and Tegaderm™ (3M Health Care, St. Paul, MN, USA), a standard dressing material, was treated to all groups. Group sizes (n=5–6 per group) were selected based on prior wound-healing studies and practical considerations[63–65]. The injection dose was limited to approximately 10 mg/kg of CN or CCN (internalized within MSCs), remaining within commonly reported tolerable ranges for silica nanoparticle administration in mice. To provide additional context regarding statistical power, we performed a post hoc power estimate based on the primary biologically relevant comparison (CCN vs control). Using our observed day-7 wound-closure data (Control: 30.7 ± 8.0; CCN: 56.9 ± 11.0; mean difference ≈ 26.2 percentage points), the post hoc analysis indicates that n=5 per group provides approximately 96% power at $\alpha = 0.05$ (two-sided) to detect the observed effect size. Animals were closely monitored following surgery for general condition, mobility, and signs of distress. Humane endpoints were predefined in accordance with institutional animal care guidelines. Animals exhibiting excessive weight loss, severe distress, or impaired mobility were humanely euthanized using CO_2 inhalation, consistent with approved protocols, to minimize suffering. The wound-healing process was monitored for up to 14 days following the initial treatments.

Histology and immunohistology

Histological analyses were conducted to confirm the therapeutic effects of MSC spheroids on the wound tissues and to evaluate the immune responses in major organs (liver, spleen, and lung) of athymic mice. Skin tissue samples were embedded in OCT compound (SciGen Scientific), then frozen and sliced into 10 μm sections at −20 °C. Organ samples were fixed with formalin, embedded in paraffin, and sliced into 5 μm sections. Under a light microscope (CKX53; Olympus), Masson's trichrome stain, hematoxylin and eosin (H&E) staining, and immunohistology stains were used to evaluate tissue regeneration and immune response in the organs. The skin tissue sections were immunostained with anti-laminin, anti-involucrin, anti-α-SMA and anti-CD31 (ab11575, ab53112, ab5694, ab28364, Abcam) with a FITC-conjugated secondary antibody (Jackson ImmunoResearch Laboratories, West Grove, PA, USA) to visualize protein expression and wound repair. All the stained sections were counterstained with DAPI (Vector Laboratories) and examined under a fluorescence microscope (Leica).

Statistics & Reproducibility

The authors declare that all data supporting the findings of this study are available in the paper and its Supplementary Information. All experiments were performed with at least three independent biological replicates unless otherwise stated. Data are presented as mean ± standard error of the mean (s.e.m.) unless otherwise indicated. No statistical method was used to predetermine sample size. Sample sizes were chosen based on commonly accepted standards in the field and prior experience with similar experimental systems. No data were excluded from the analyses. Samples were allocated into experimental groups based on predefined experimental conditions. Investigators were blinded to group allocation during data collection and analysis. Animals were randomly assigned to experimental groups in the mouse wound healing model. For comparisons between two groups, two-sided unpaired Student's t-tests were used. For comparisons involving more than two groups, one-way analysis of variance (ANOVA) followed by Tukey's multiple comparisons test was applied, unless otherwise specified. Exact p-values are reported in the figure legends where applicable. Statistical analyses were performed using GraphPad Prism version 9 software. A p-value of less than 0.05 was considered statistically significant.

Data availability

The data supporting the findings of this study are available within the main text, figures, and Supplementary Information. The bulk RNA sequencing dataset associated with CN, CCN, and NT experimental groups has been deposited in the Gene Expression Omnibus under accession number "GSE328760 [https://www.ncbi.nlm.nih.gov/geo/query/acc.cgi?acc=GSE328760]". Any additional requests for information can be directed to, and will be fulfilled by, the corresponding authors. Source data are provided with this paper.

References

1. Mathiasen, A. B. *et al.* Bone marrow-derived mesenchymal stromal cell treatment in patients with severe ischaemic heart failure: a randomized placebo-controlled trial (MSC-HF trial). *Eur. Hear. J.* **36**, 1744–1753 (2015).

2. Bartolucci, J. *et al.* Safety and Efficacy of the Intravenous Infusion of Umbilical Cord Mesenchymal Stem Cells in Patients With Heart Failure. *Circ. Res.* **121**, 1192–1204 (2017).

3. Hicks, M. R. *et al.* Regenerating human skeletal muscle forms an emerging niche in vivo to support PAX7 cells. *Nat. Cell Biol.* **25**, 1758–1773 (2023).

4. Mitrousis, N., Fokina, A. & Shoichet, M. S. Biomaterials for cell transplantation. *Nat. Rev. Mater.* **3**, 441–456 (2018).

5. Mastrolia, I. *et al.* Challenges in Clinical Development of Mesenchymal Stromal/Stem Cells: Concise Review. *STEM CELLS Transl. Med.* **8**, 1135–1148 (2019).

6. Kou, M. *et al.* Mesenchymal stem cell-derived extracellular vesicles for immunomodulation and regeneration: a next generation therapeutic tool? *Cell Death Dis.* **13**, 580 (2022).

7. Adebowale, K. *et al.* Enhanced substrate stress relaxation promotes filopodia-mediated cell migration. *Nat. Mater.* **20**, 1290–1299 (2021).

8. Huang, D. *et al.* Collagen hydrogel viscoelasticity regulates MSC chondrogenesis in a ROCK-dependent manner. *Sci. Adv.* **9**, eade9497 (2023).

9. Trappmann, B. *et al.* Extracellular-matrix tethering regulates stem-cell fate. *Nat. Mater.* **11**, 642–649 (2012).

10. Fajrial, A. K., He, Q. Q., Wirusanti, N. I., Slansky, J. E. & Ding, X. A review of emerging physical transfection methods for CRISPR/Cas9-mediated gene editing. *Theranostics* **10**, 5532–5549 (2020).

11. Chen, Q. *et al.* Dual mechanism β-amino acid polymers promoting cell adhesion. *Nat Commun* **12**, 562 (2021).

12. Liu, K., Yu, C., Xie, M., Li, K. & Ding, S. Chemical Modulation of Cell Fate in Stem Cell Therapeutics and Regenerative Medicine. *Cell Chem. Biol.* **23**, 893–916 (2016).

13. Aussel, C., Cathomen, T. & Fuster-García, C. The hidden risks of CRISPR/Cas: structural variations and genome integrity. *Nat. Commun.* **16**, 7208 (2025).

14. Martin, R. M. *et al.* Improving the safety of human pluripotent stem cell therapies using genome-edited orthogonal safeguards. *Nat. Commun.* **11**, 2713 (2020).

15. Im, G.-B. *et al.* 2D and 3D co-spatial compartmentalized patch to enhance the therapeutic efficacy of keratinocytes for wound closure. *Chem. Eng. J.* **409**, 128130 (2021).

16. Cheng, K. *et al.* Magnetic Targeting Enhances Engraftment and Functional Benefit of Iron-Labeled Cardiosphere-Derived Cells in Myocardial Infarction. *Circ. Res.* **106**, 1570–1581 (2010).

17. Li, Y. *et al.* Elastic porous microspheres/extracellular matrix hydrogel injectable composites releasing dual bio-factors enable tissue regeneration. *Nat. Commun.* **15**, 1377 (2024).

18. Lu, P. *et al.* Harnessing the potential of hydrogels for advanced therapeutic applications: current achievements and future directions. *Signal Transduct. Target. Ther.* **9**, 166 (2024).

19. Feric, M. & Brangwynne, C. P. A nuclear F-actin scaffold stabilizes ribonucleoprotein droplets against gravity in large cells. *Nat. Cell Biol.* **15**, 1253–1259 (2013).

20. Whitcome, K. K., Shapiro, L. J. & Lieberman, D. E. Fetal load and the evolution of lumbar lordosis in bipedal hominins. *Nature* **450**, 1075–1078 (2007).

21. Tan, T. H. *et al.* Odd dynamics of living chiral crystals. *Nature* **607**, 287–293 (2022).

22. Hajizadeh, K., Mehdian, H., Hajisharifi, K. & Robert, E. A van der Waals force-based adhesion study of stem cells exposed to cold atmospheric plasma jets. *Sci. Rep.* **12**, 12069 (2022).

23. Parsons, J. T., Horwitz, A. R. & Schwartz, M. A. Cell adhesion: integrating cytoskeletal dynamics and cellular tension. *Nat. Rev. Mol. Cell Biol.* **11**, 633–643 (2010).

24. Davis, T. *et al.* How are cell and tissue structure and function influenced by gravity and what are the gravity perception mechanisms? *npj Microgravity* **10**, 16 (2024).

25. Lancaster, O. M. *et al.* Mitotic Rounding Alters Cell Geometry to Ensure Efficient Bipolar Spindle Formation. *Dev. Cell* **25**, 270–283 (2013).

26. Chin, J. S. *et al.* Secretome from prolonged high-density human Wharton's jelly stem cell culture accelerates wound healing in both in vitro and in vivo models. *Int. Wound J.* **22**, e70033 (2025).

27. Alonso-Matilla, R., Provenzano, P. P. & Odde, D. J. Physical principles and mechanisms of cell migration. *npj Biol. Phys. Mech.* **2**, 2 (2025).

28. Discher, D. E., Mooney, D. J. & Zandstra, P. W. Growth Factors, Matrices, and Forces Combine and Control Stem Cells. *Science* **324**, 1673–1677 (2009).

29. Gu, Z. *et al.* S-Nitrosylation of Matrix Metalloproteinases: Signaling Pathway to Neuronal Cell Death. *Science* **297**, 1186–1190 (2002).

30. Muenzner, P., Bachmann, V., Zimmermann, W., Hentschel, J. & Hauck, C. R. Human-Restricted Bacterial Pathogens Block Shedding of Epithelial Cells by Stimulating Integrin Activation. *Science* **329**, 1197–1201 (2010).

31. Neurohr, G. E. & Amon, A. Relevance and Regulation of Cell Density. *Trends Cell Biol.* **30**, 213–225 (2020).

32. Lerman, M. J., Lembong, J., Muramoto, S., Gillen, G. & Fisher, J. P. The Evolution of Polystyrene as a Cell Culture Material. *Tissue Eng. Part B: Rev.* **24**, 359–372 (2018).

33. Mahdian, S. M. A. *et al.* Plasma treatment can efficiently increase the attachment of pancreatic circulatory tumor cells to the surface. *Discov. Oncol.* **16**, 222 (2025).

34. Im, G. *et al.* Ceria Nanoparticles as Copper Chaperones that Activate SOD1 for Synergistic Antioxidant Therapy to Treat Ischemic Vascular Diseases. *Adv. Mater.* **35**, e2208989 (2023).

35. Beenken, A. & Mohammadi, M. The FGF family: biology, pathophysiology and therapy. *Nat. Rev. Drug Discov.* **8**, 235–253 (2009).

36. Weber, M.-C. *et al.* Fractal analysis of extracellular matrix for observer-independent quantification of intestinal fibrosis in Crohn’s disease. *Sci. Rep.* **14**, 3988 (2024).

37. Das, A. *et al.* Cysteine oxidation of copper transporter CTR1 drives VEGFR2 signalling and angiogenesis. *Nat. Cell Biol.* **24**, 35–50 (2022).

38. Brady, D. C. *et al.* Copper is required for oncogenic BRAF signalling and tumorigenesis. *Nature* **509**, 492–496 (2014).

39. Lei, Q. *et al.* Extracellular vesicles deposit PCNA to rejuvenate aged bone marrow–derived mesenchymal stem cells and slow age-related degeneration. *Sci. Transl. Med.* **13**, (2021).

40. Chen, L. *et al.* Structural basis for FGF hormone signalling. *Nature* **618**, 862–870 (2023).

41. Krężel, A. & Maret, W. The Bioinorganic Chemistry of Mammalian Metallothioneins. *Chem. Rev.* **121**, 14594–14648 (2021).

42. Taha, H. *et al.* Role of Heme Oxygenase-1 in Human Endothelial Cells. *Arter., Thromb., Vasc. Biol.* **30**, 1634–1641 (2010).

43. Lenhart, P. M. & Caron, K. M. Adrenomedullin and pregnancy: perspectives from animal models to humans. *Trends Endocrinol. Metab.* **23**, 524–532 (2012).

44. Ponta, H., Sherman, L. & Herrlich, P. A. CD44: From adhesion molecules to signalling regulators. *Nat. Rev. Mol. Cell Biol.* **4**, 33–45 (2003).

45. Zhu, H. *et al.* The Role of the Hyaluronan Receptor CD44 in Mesenchymal Stem Cell Migration in the Extracellular Matrix. *STEM CELLS* **24**, 928–935 (2006).

46. Tian, M. *et al.* JLP/Foxk1/N-cadherin axis fosters a partial epithelial-mesenchymal transition state in epithelial tubular cells. *iScience* **26**, 106396 (2023).

47. Doble, B. W., Ping, P. & Kardami, E. The ε Subtype of Protein Kinase C Is Required for Cardiomyocyte Connexin-43 Phosphorylation. *Circ. Res.* **86**, 293–301 (2000).

48. Hamidouche, Z. *et al.* Priming integrin α5 promotes human mesenchymal stromal cell osteoblast differentiation and osteogenesis. *Proc. Natl. Acad. Sci.* **106**, 18587–18591 (2009).

49. Pan, R. *et al.* Low-molecular-weight fibroblast growth factor 2 attenuates hepatic fibrosis by epigenetic down-regulation of Delta-like1. *Hepatology* **61**, 1708–1720 (2015).

50. Aguilera-Correa, J. J. *et al.* In vivo antimicrobial activity of engineered mesoporous silica nanoparticles targeting intracellular mycobacteria. *Nat. Commun.* **16**, 7388 (2025).

51. Nguyen, B. L. *et al.* Binary mineral nanoparticles enable intravascular delivery of metal ions to tumors for metalloimmunotherapy. *Nat. Commun.* **17**, 1556 (2026).

52. Leon, G. D. *et al.* An ultrasmall core–shell silica nanoparticle improves antitumour immunity and survival by remodelling suppressive melanoma microenvironments. *Nat. Nanotechnol.* **21**, 311–322 (2026).

53. Dunn, L. *et al.* Murine Model of Wound Healing. *J. Vis. Exp.* e50265 (2013) doi:10.3791/50265.

54. Andres, J. D. *et al.* Intrathecal Drug Delivery: Advances and Applications in the Management of Chronic Pain Patient. *Front. Pain Res.* **3**, 900566 (2022).

55. Eckert, J., Loon, J. J. W. A. van, Eng, L. M. & Schmidt, T. Hypergravity affects cell traction forces of fibroblasts. *Biophys. J.* **120**, 773–780 (2021).

56. Rustad, K. C. & Gurtner, G. C. Mesenchymal Stem Cells Home to Sites of Injury and Inflammation. *Adv. Wound Care* **1**, 147–152 (2011).

57. Han, X. *et al.* Mesenchymal stem cells in treating human diseases: molecular mechanisms and clinical studies. *Signal Transduct. Target. Ther.* **10**, 262 (2025).

58. Janjua, T. I., Cao, Y., Yu, C. & Popat, A. Clinical translation of silica nanoparticles. *Nat. Rev. Mater.* **6**, 1072–1074 (2021).

59. Yoo, H. & Pak, J. Synthesis of highly fluorescent silica nanoparticles in a reverse microemulsion through double-layered doping of organic fluorophores. *J. Nanoparticle Res.* **15**, 1609 (2013).

60. Im, G.-B., Kim, S.-W. & Bhang, S. H. Fortifying the angiogenic efficacy of adipose derived stem cell spheroids using spheroid compaction. *J. Ind. Eng. Chem.* **93**, 228–236 (2021).

61. Han, J. *et al.* Development of Zinc-Containing Chitosan/Gelatin Coatings with Immunomodulatory Effect for Soft Tissue Sealing around Dental Implants. *Tissue Eng. Regen. Med.* **22**, 57–75 (2025).

62. Kim, C. Y., Jeong, C., Han, Y. & Hwang, C. Angiopoietin-1 and Tie2-Based Dual Cell Therapy Enhances Antiangiogenic Barrier Function in a Retina-Mimetic Model for Neovascular Retinal Disease. *Tissue Eng. Regen. Med.* **22**, 877–893 (2025).

63. Baek, S.-W. *et al.* Bulk Modification with Inorganic Particles and Immobilization of Extracellular Vesicles onto PDO Composite for Facial Rejuvenation. *Tissue Eng. Regen. Med.* **21**, 199–208 (2024).

64. Kim, Y. H. *et al.* Tri-layer hydrogel scaffold supporting co-culture paracrine signaling for accelerated skin repair. *J. Ind. Eng. Chem.* (2025) doi:10.1016/j.jiec.2025.08.021.

65. Vågesjö, E. *et al.* Accelerated wound healing in mice by on-site production and delivery of CXCL12 by transformed lactic acid bacteria. *Proc. Natl. Acad. Sci.* **115**, 1895–1900 (2018).

66. Ishi, S. *et al.* Cutaneous wound healing promoted by topical administration of heat-killed Lactobacillus plantarum KB131 and possible contribution of CARD9-mediated signaling. *Sci. Rep.* **13**, 15917 (2023).

67. Cho, C.-H. *et al.* COMP-angiopoietin-1 promotes wound healing through enhanced angiogenesis, lymphangiogenesis, and blood flow in a diabetic mouse model. *Proc. Natl. Acad. Sci.* **103**, 4946–4951 (2006).

Funding

S.H.B discloses support for the research of this work from the Korean Fund for Regenerative Medicine (KFRM) grant (KFRM 21A0102L1-22, KFRM 25A0105L1), funded by the Ministry of Science and ICT, Republic of Korea. This work is also supported by the Alchemist Project of the Korea Evaluation Institute of Industrial Technology (KEIT 20018560, NTIS 2410005252), the Ministry of Trade, Industry & Energy, Republic of Korea. S.H.B also discloses support for the research of this work from the National Research Foundation of Korea (NRF) grant funded by the Korea government (MSIT) (No. RS-2024-00405818). This work was supported by the Technology Innovation Program (RS-2024-00434908, Development of a wearable light irradiation device for active drug release and wound treatment using stretchable light-emitting devices) funded By the Ministry of Trade Industry & Energy (MOTIE, Korea). J.W.B. declares no relevant funding.

Author contributions

H.S.P. and G.-B.I., J.W.B, and S.H.B conceived, designed, and led the study. H.S.P., G.-B.I., S.Y.J., J.S.L., J.H.L., S.-W.K., J.H., Y.-J.J., and E.-C.L. performed the experiments. H.S.P., G.-B.I., A.F., J.S.L., J.H.L., and Y.L. analyzed the data. H.S.P., G.-B.I., J.W.B., and S.H.B wrote the manuscript.

Competing interests

The authors declare no competing interests

Figure legends

Fig. 1. Cell-settling nanoparticles are designed to improve cell adhesion and retention via increased gravitational force, while enhancing the therapeutic effects through copper-driven FGF2 expression. a, Internalization of CN or CCN increases cell mass and density, thereby accelerating gravitational sinking and enhancing cell adhesion efficiency. **b,** CCN development from CN to increase copper chaperone activation and vascularization with FGF2 positive feedback loop triggered by extracellular signal-regulated kinase (ERK) cascade. Created in BioRender. Im, G. (2026) https://BioRender.com/j2focno

Fig. 2. Synthesis of CN and their role in accelerating cell settling speed through enhanced gravitational force. a, Schematic figure of enhanced cell adhesion via CN internalization. **b,** TEM images of synthesized CN showing uniform size. **c,** Representative fluorescence image showing the internalization of CN (Rhodamine, red) into MSCs (green). Scale bar indicates 100 µm. **d,** Relative cell viability compared to normal (0 µg/mL) cells at 24 h after CN treatment evaluated by CCK-8 assay. (n = 4; one-way ANOVA followed by Tukey's multiple comparisons test; mean ± s.d.). **e,** Changes in cell density based on the treatment time and concentration of CN, indicating that higher concentrations of CN lead to increased cell density. P values were determined from comparisons between connected groups (n = 7; unpaired two-tailed t-test; mean ± s.d.). **f,** Simulation of changes in displacement based on the concentration of CN. **g,** Graph showing normalized displacement over time at different concentrations of CN. **h,** Schematic of the method comparing cell-settling speed between the NT (Non-treated) and CN groups. **i,** FACS analysis of PE-positive NT (blue) and CN (red) showing the proportion of cells with a faster sinking rate. **j,** Representative image showing increased cell adhesion at 6 h after CN treatment. Scale bar indicates 200 µm. **k,** Relative ratio of attached cells compared to the NT group. P value was determined from comparisons between connected groups (n = 4, unpaired two-tailed t-test; mean ± s.d.). Created in BioRender. Im, G. (2026) https://BioRender.com/ubtt5m4

Fig. 3. Copper-chaperone-activatable cell-settling nanoparticles (CCN) derived from CN, designed to enhance MSC retention at the target site. a, Schematic figure of enhanced cell

adhesion via CCN internalization. **b,** TEM images of synthesized CCN showing uniform diameter. **c,** Relative cellular complexity of various groups. P values were determined from comparisons between connected groups (n = 4; one-way ANOVA followed by Tukey's multiple comparisons test; mean ± s.d.). **d,** Representative image showing increased cell adhesion at 6 h after CN and CCN treatment. Scale bar indicates 200 μm. **e,** Relative ratio of attached cells compared to the NT group. P values were determined from comparisons between connected groups (n = 6; one-way ANOVA followed by Tukey's multiple comparisons test; mean ± s.d.). **f,** Western blot analysis of relative expression of adhesion protein from various groups at 24 h after cell attachment. P values were determined from comparisons between connected groups (n = 4; one-way ANOVA followed by Tukey's multiple comparisons test; mean ± s.d.). For CD44, a pairwise comparison between NT and CCN groups showed P = 0.0153 (n = 4; unpaired two-tailed t-test; mean ± s.d.). **g,** Relative radiant efficiency after the cell injection with or without CN or CCN treatment into the wound site. P values were determined from comparisons between connected groups (n = 4; one-way ANOVA followed by Tukey's multiple comparisons test; mean ± s.d.). **h,** *In vivo* fluorescence images indicating the retention of injected cells over time. Created in BioRender. Im, G. (2026) https://BioRender.com/m13oyw6

Fig. 4. Cell aggregate culture with increased cell density using CN or CCN. a, Schematic illustration showing that the aggregation rate depends on the single-cell density. **b**, Fluorescence image showing enhanced early time MSCs aggregation in CN and CCN groups. Scale bar indicates 500 μm. **c,** Relative area occupied by cells in each group during aggregate formation, showing faster aggregation in CN- or CCN-treated groups compared to NT. P values were determined from comparisons between connected groups (n = 6; one-way ANOVA followed by Tukey's multiple comparisons test; mean ± s.d.). Relative expression of adhesion-related genes **d,** 1 h or **e,** 3 h after the cell aggregation. P values were determined from comparisons between connected groups (n = 4; one-way ANOVA followed by Tukey's multiple comparisons test; mean ± s.d.). **f,** Western blot data showing the adhesion-related protein expression. P values were determined from comparisons between connected groups (n = 4; one-way ANOVA followed by Tukey's multiple comparisons test; mean ± s.d.). Created in BioRender. Im, G. (2026) https://BioRender.com/ss48hmv

Fig. 5. MSC aggregates internalized with CCN exhibit superior wound healing efficacy compared to CN and control groups. a, Schematic of the *in vivo* test timeline. **b,** Wound closure ratio up to day 14. P values were determined from comparisons between connected groups (n = 5; one-way ANOVA followed by Tukey's multiple comparisons test; mean ± s.d.). **c,** Representative image showing the trend of wound healing up to day 14. **d,** Immunofluorescent staining for mouse-involucrin (green), laminin (green), α-SMA (green), and CD31 (green) at day 14. Scale bar indicates 200 and 100 μm. **e,** Relative gene expression of *Ivl*, *Pecam1*, and *Acta2* at the wound site. P values were determined from comparisons between connected groups (n = 4; one-way ANOVA followed by Tukey's multiple comparisons test; mean ± s.d.). **f,** Relative gene expression of *Col1a1* and *Acata2*/*Pecam1* at wound site. P values were determined from comparisons between connected groups (n = 4; one-way ANOVA followed by Tukey's multiple comparisons test; mean ± s.d.). **g,** Masson's trichrome staining after various treatments. Scale bar indicates 500 μm**. h,** Analysis of the relative amount of collagen (blue) at the wound site after Masson's trichrome staining. P values were determined from comparisons between connected groups (n = 4; one-way ANOVA followed by Tukey's multiple comparisons test; mean ± s.d.). Western blot data showing **i,** Col3A1 and Col1A1 protein expression, **j,** relative expression of Col3A1/Col1A1 and Col3A1. P values were determined from comparisons between connected groups (n = 4; one-way ANOVA followed by Tukey's multiple comparisons test; mean ± s.d.). Created in BioRender. Im, G. (2026) https://BioRender.com/hqm6lrf

Fig. 6. FGF2 signaling occurs by a positive feedback loop after CCN treatment. a, Schematic of FGF2 signaling and inhibitors. **b, c** Western blot data showing protein expression of pMEK, MEK, pERK, ERK, FGF2, and PCNA. P values were determined from comparisons between connected groups (n = 4; one-way ANOVA followed by Tukey's multiple comparisons test; mean ± s.d.). **d,** Relative protein expression of CCS at 1 h after CN or CCN treatment. P value was determined from comparisons between connected groups (n = 4; one-way ANOVA followed by Tukey's multiple comparisons test; mean ± s.d.). **e,** Relative gene expression of CCS, ERK, and FGF2 during cell aggregation. P values were determined from comparisons between connected

group (n = 4; one-way ANOVA followed by Tukey's multiple comparisons test; mean ± s.d.). **f,** Relative protein expression of pERK/ERK ratio and FGF2 after FGF2 inhibitor (FGF2i) or ERK inhibitor (ERKi) treatment. P values were determined from comparisons between connected groups (n = 4; one-way ANOVA followed by Tukey's multiple comparisons test; mean ± s.d.). Relative gene expressions of **g,** FGF2 and **h,** CCS during cell aggregation with CCS inhibitor. P values were determined from comparisons between connected groups (n = 4, unpaired two-tailed t-test; mean ± s.d.). **i,** Representative images showing the FGF2 (green) expression. Scale bar indicates 100 μm. Created in BioRender. Im, G. (2026) https://BioRender.com/yhhbxt1

Fig. 7. Transcriptomic analysis and proposed mechanism of CCN-mediated cellular reprogramming. a, Schematic illustration of the proposed mechanism following CCN internalization, highlighting enhanced FGF2 signaling, angiogenesis, and anti-fibrosis. **b,** Heatmap showing differentially expressed genes of each group. **c,** Gene Ontology (GO) enrichment analysis of DEGs identified in CN and CCN relative to NT, revealing biological processes associated with the ERK1/2 cascade, wound healing, and copper ion response. **d,** GO terms exhibiting differential enrichment between CN and CCN relative to NT. **e,** KEGG pathway enrichment analysis of DEGs identified in CN and CCN relative to NT, including MAPK, PI3K-Akt, and Rap1 signaling cascades. **f,** Pathway terms exhibiting differential enrichment between CN and CCN relative to NT. **g,** Volcano plot of DEGs in the CN and CCN relative to NT, highlighting that FGF2 and several metallothionein genes upregulated in CCN.

Fig. 8. *In vitro* wound healing efficacy of CN or CCN internalized MSCs aggregate. a, Schematic illustration of the experiment using SP culture medium (CM). **b-d**, Wound scratch assay after CM treatment extracted from various groups: **b,** quantification of cell migration efficiency (n = 5), **c,** representative image of cell migration at 0 and 24 h (Scale bar indicates 500 μm), and **d,** relative CXCR4 expression (n = 4) at 24 h after the various treatment. P values were determined from comparisons with Control (CM-untreated group) (n = 4; one-way ANOVA followed by Tukey's multiple comparisons test; mean ± s.d.). **e,** Myofibroblast differentiation after TGF-β treatment to fibroblasts with CM extracted from various groups. Scale bar indicates 50 μm. **f,** Gene

expression related to fibrosis in various groups. **g,** Tube formation of HUVECs after CM treatment extracted from various groups. Scale bar indicates 250 µm. **h,** Relative number of nodes and meshes quantified from tube formation assay data. P values were determined from comparisons between connected groups (n = 4; one-way ANOVA followed by Tukey's multiple comparisons test; mean ± s.d.). Created in BioRender. Im, G. (2026) https://BioRender.com/0s48wpj

Editorial Summary:

Low retention of transplanted stem cells limits their clinical application. Here, the authors develop a nanoparticle-based strategy that increases cell density to enhance retention, improve tissue regeneration, and reduce fibrosis through modulation of cellular density and physical forces.

Peer Review Information: *Nature Communications* thanks Ali Zarrabi, Jered Haun and Oleksandra Fanari for their contribution to the peer review of this work. A peer review file is available."

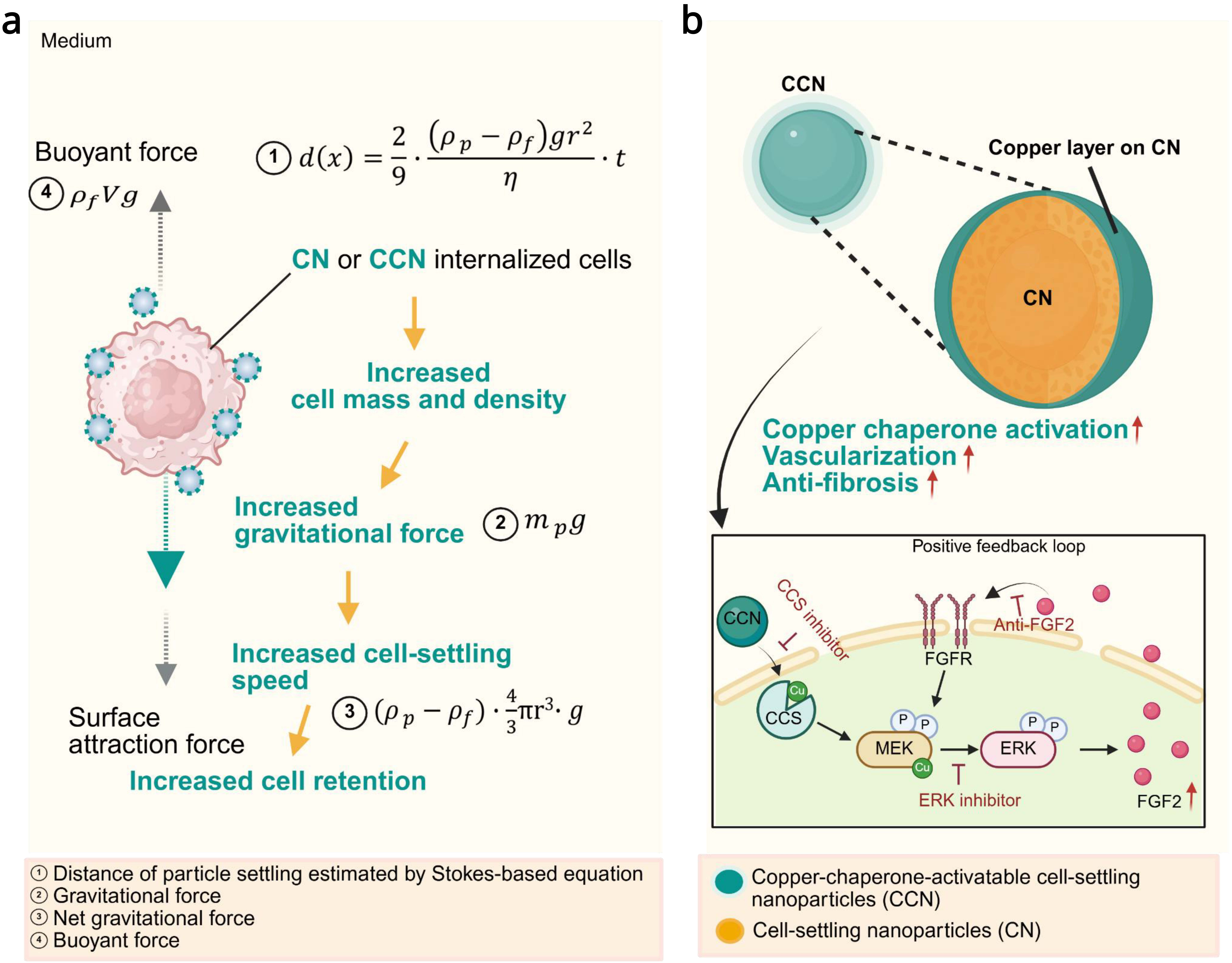
a
Medium
Buoyant force
④ $\rho_f V g$
① $d(x) = \frac{2}{9} \cdot \frac{(\rho_p - \rho_f) g r^2}{\eta} \cdot t$
CN or CCN internalized cells
Increased cell mass and density
Increased gravitational force
② $m_p g$
Increased cell-settling speed
③ $(\rho_p - \rho_f) \cdot \frac{4}{3}\pi r^3 \cdot g$
Surface attraction force
Increased cell retention
① Distance of particle settling estimated by Stokes-based equation
② Gravitational force
③ Net gravitational force
④ Buoyant force
b
CCN
Copper layer on CN
CN
Copper chaperone activation ↑
Vascularization ↑
Anti-fibrosis ↑
Positive feedback loop
CCN
CCS inhibitor
FGFR
Anti-FGF2
Cu
CCS
P
P
MEK
Cu
ERK
P
P
ERK inhibitor
FGF2 ↑
Copper-chaperone-activatable cell-settling nanoparticles (CCN)
Cell-settling nanoparticles (CN)

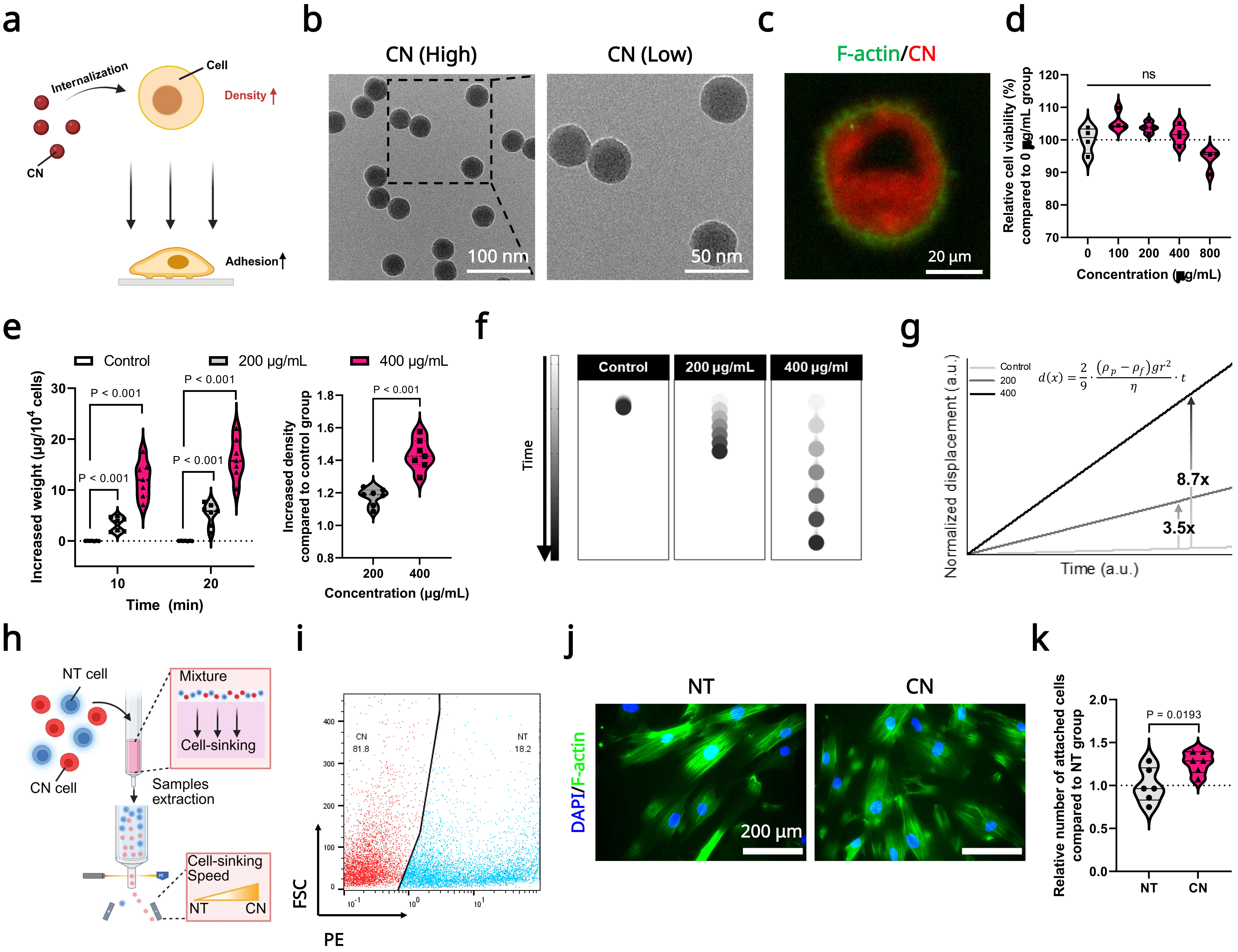
a
Internalization
Cell
Density ↑
CN
Adhesion ↑
b
CN (High)
CN (Low)
100 nm
50 nm
c
F-actin/CN
20 µm
d
ns
Relative cell viability (%) compared to 0 µg/mL group
120
110
100
90
80
70
0
100
200
400
800
Concentration (µg/mL)
e
Control
200 µg/mL
400 µg/mL
P < 0.001
P < 0.001
P < 0.001
P < 0.001
Increased weight (µg/10⁴ cells)
30
20
10
0
10
20
Time (min)
P < 0.001
Increased density compared to control group
1.8
1.6
1.4
1.2
1.0
0.8
200
400
Concentration (µg/mL)
f
Time
Control
200 µg/mL
400 µg/ml
g
Control
200
400
$d(x) = \frac{2}{9} \cdot \frac{(\rho_p - \rho_f)gr^2}{\eta} \cdot t$
8.7x
3.5x
Normalized displacement (a.u.)
Time (a.u.)
h
NT cell
CN cell
Mixture
Cell-sinking
Samples extraction
Cell-sinking Speed
NT
CN
i
CN
81.8
NT
18.2
400
300
200
100
0
10⁻¹
10⁰
10¹
FSC
PE
j
NT
CN
DAPI/F-actin
200 µm
k
P = 0.0193
Relative number of attached cells compared to NT group
2.0
1.5
1.0
0.5
0.0
NT
CN

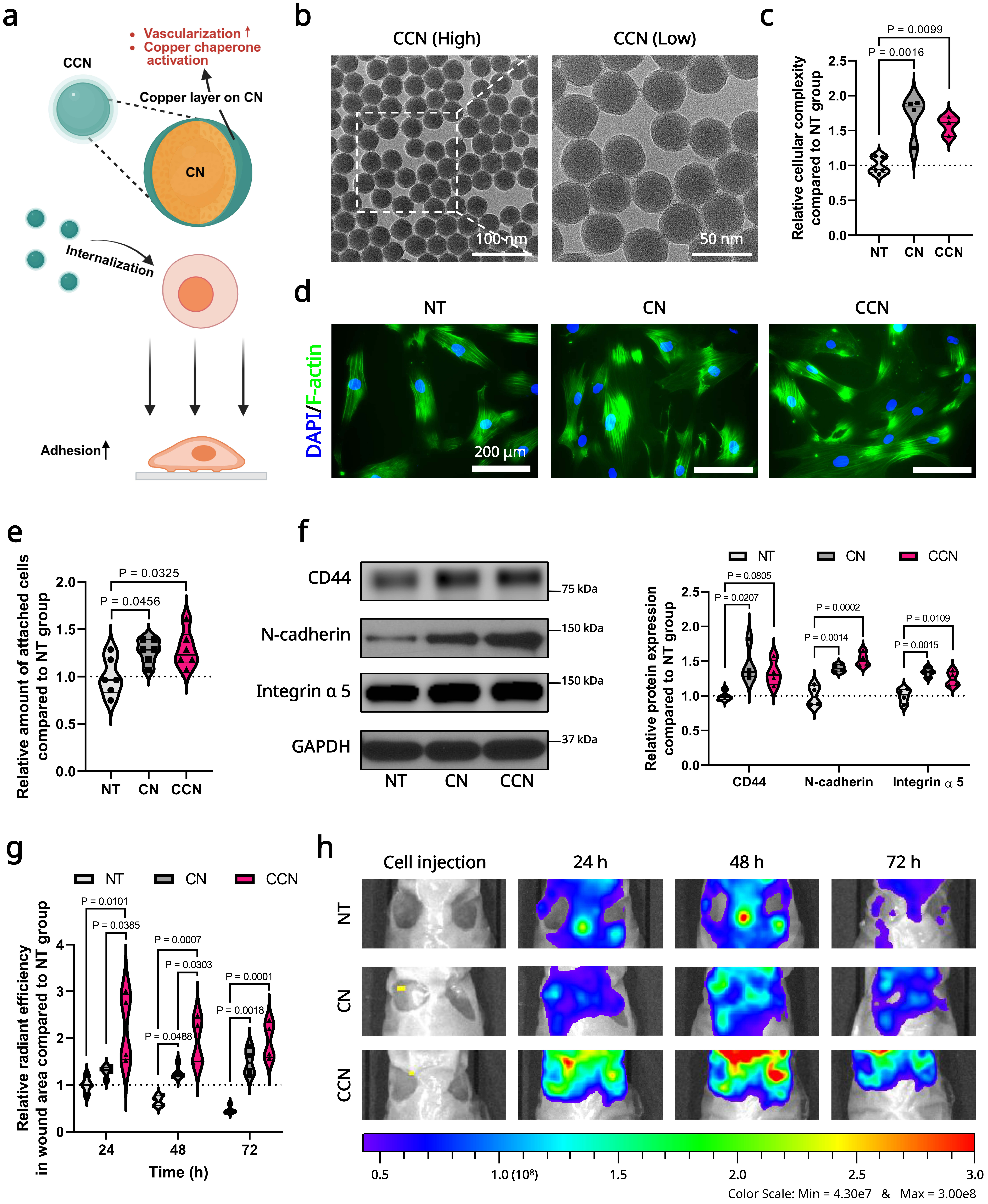
a
Vascularization ↑
Copper chaperone activation
CCN
Copper layer on CN
CN
Internalization
Adhesion ↑
b
CCN (High)
CCN (Low)
100 nm
50 nm
c
P = 0.0099
P = 0.0016
Relative cellular complexity compared to NT group
2.5
2.0
1.5
1.0
0.5
0.0
NT
CN
CCN
d
NT
CN
CCN
DAPI/F-actin
200 μm
e
P = 0.0325
P = 0.0456
Relative amount of attached cells compared to NT group
2.0
1.5
1.0
0.5
0.0
NT
CN
CCN
f
CD44
75 kDa
N-cadherin
150 kDa
Integrin α 5
150 kDa
GAPDH
37 kDa
NT
CN
CCN
NT
CN
CCN
P = 0.0805
P = 0.0207
P = 0.0002
P = 0.0014
P = 0.0109
P = 0.0015
Relative protein expression compared to NT group
2.5
2.0
1.5
1.0
0.5
0.0
CD44
N-cadherin
Integrin α 5
g
NT
CN
CCN
P = 0.0101
P = 0.0385
P = 0.0007
P = 0.0303
P = 0.0488
P = 0.0001
P = 0.0018
Relative radiant efficiency in wound area compared to NT group
4
3
2
1
0
24
48
72
Time (h)
h
Cell injection
24 h
48 h
72 h
NT
CN
CCN
0.5
1.0 (10⁸)
1.5
2.0
2.5
3.0
Color Scale: Min = 4.30e7 & Max = 3.00e8

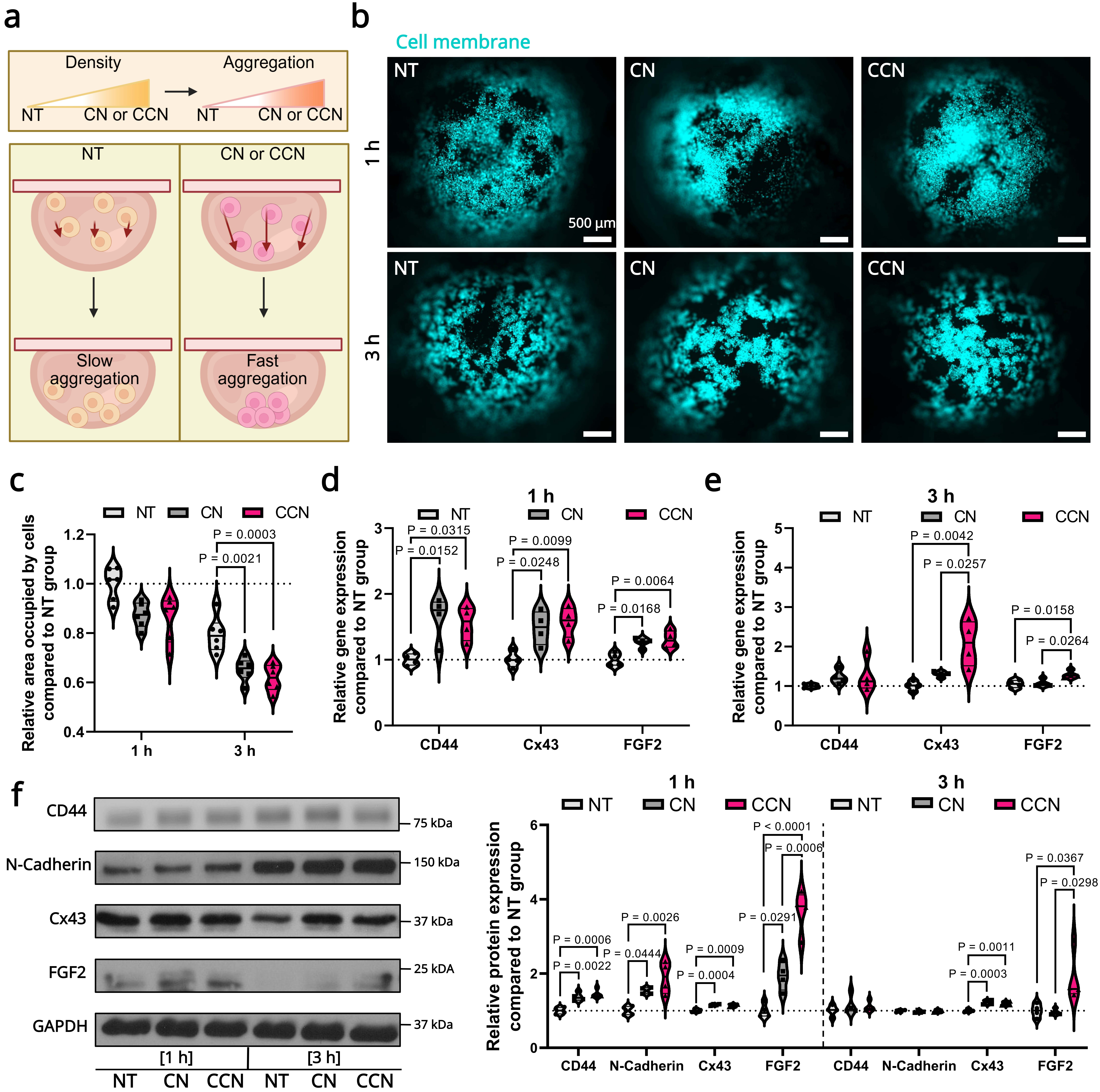
a
Density
Aggregation
NT
CN or CCN
NT
CN or CCN
NT
CN or CCN
Slow aggregation
Fast aggregation
b
Cell membrane
1 h
3 h
NT
CN
CCN
500 μm
c
NT
CN
CCN
Relative area occupied by cells compared to NT group
1.2
1.0
0.8
0.6
0.4
P = 0.0003
P = 0.0021
1 h
3 h
d
1 h
NT
CN
CCN
Relative gene expression compared to NT group
3
2
1
0
P = 0.0315
P = 0.0152
P = 0.0099
P = 0.0248
P = 0.0064
P = 0.0168
CD44
Cx43
FGF2
e
3 h
NT
CN
CCN
Relative gene expression compared to NT group
5
4
3
2
1
0
P = 0.0042
P = 0.0257
P = 0.0158
P = 0.0264
CD44
Cx43
FGF2
f
CD44
75 kDa
N-Cadherin
150 kDa
Cx43
37 kDa
FGF2
25 kDA
GAPDH
37 kDa
[1 h]
[3 h]
NT
CN
CCN
NT
CN
CCN
1 h
3 h
NT
CN
CCN
NT
CN
CCN
Relative protein expression compared to NT group
6
4
2
0
P = 0.0006
P = 0.0022
P = 0.0026
P = 0.0444
P = 0.0009
P = 0.0004
P < 0.0001
P = 0.0006
P = 0.0291
P = 0.0011
P = 0.0003
P = 0.0367
P = 0.0298
CD44
N-Cadherin
Cx43
FGF2
CD44
N-Cadherin
Cx43
FGF2


a
Day -1
Day 0
Day 14
SP Formation
Skin wound mouse model & cell injection
Analysis
-Wound Closure ratio
-qRT-PCR
-Histology
Group | Control | NT | CN | CCN
Cell | No treat | MSCs | MSCs | MSCs
NPs | No treat | No treat | CNs | CCNs
b
Control
NT
CN
CCN
Wound healing ratio
Occupied area / initial wound area, (%)
Day
P = 0.0011
P = 0.0376
P = 0.0119
P = 0.0007
P = 0.0109
P = 0.0054
P = 0.0054
P = 0.0133
P = 0.0236
Day 14
P < 0.0001
P = 0.0054
P = 0.0133
P < 0.0236
c
Control
NT
CN
CCN
Day 0
Day 3
Day 7
Day 10
Day 14
d
Control
NT
CN
CCN
DAPI/Involucrin
DAPI/Laminin
DAPI/α-SMA
DAPI/CD31
200 μm
200 μm
100 μm
100 μm
e
Ivl
Pecam1
Acta2
Relative gene expression compared to Control group
P = 0.0153
P = 0.0073
P = 0.0095
P = 0.0238
P = 0.0103
P = 0.0056
f
Col1a1
Acta2/Pecam1
Relative gene expression compared to Control group
Relative Acta2/Pecam1 ratio compared to Control group
P = 0.0080
P = 0.0422
P = 0.0124
P = 0.0098
g
Control
NT
CN
CCN
500 μm
h
Relative persentage of collagen compared to NT group
P < 0.0001
P < 0.0001
P < 0.0001
P < 0.0001
P = 0.0007
i
Col3A1
Col1A1
β-Actin
150 kDa
150 kDa
37 kDa
Ct
NT
CN
CCN
j
Col3A1/Col1A1
Col3A1
Relative protein expression compared to Control group
P = 0.0003
P < 0.0001
P = 0.0001
P = 0.0042
P = 0.0072
Control
NT
CN
CCN


a
Positive feedback loop
CCN
CCS inhibitor
Cu
CCS
FGFR
Anti-FGF2
P
P
MEK
Cu
ERK
ERK inhibitor
FGF2
b
pMEK
MEK
pERK
ERK
FGF2
PCNA
GAPDH
37 kDa
26 kDa
NT CN CCN
c
pMEK/MEK
P = 0.0111
P = 0.0204
pERK/ERK
P = 0.0018
P = 0.0029
FGF2
P < 0.0001
P = 0.0237
P = 0.0045
PCNA
P = 0.0012
P = 0.0070
Relative protein expression compared to NT group
NT CN CCN
d
CCS 1h
P = 0.0103
ns
Relative protein expression compared to NT SP group
e
CCS 24h
P = 0.0466
ERK 24h
P = 0.0495
FGF2 24h
P = 0.0003
P = 0.0006
Relative gene expression compared to NT group
Relative gene expression compared to NT SP group
f
pERK/ERK
P < 0.0001
P < 0.0001
FGF2
P = 0.0009
P = 0.0012
Relative protein expression compared to NT group
NT FGF2i ERKi
g
FGF2
P = 0.0021
P = 0.0026
P = 0.0388
P = 0.0125
Relative gene expression compared to NT-X group
CCS inhibitor X O X O X O
Group NT CN CCN
h
CCS
P = 0.0056
P = 0.0020
P = 0.0025
P = 0.0197
i
NT
CN
CCN
DAPI/F-actin/FGF2
100 µm
FGF2

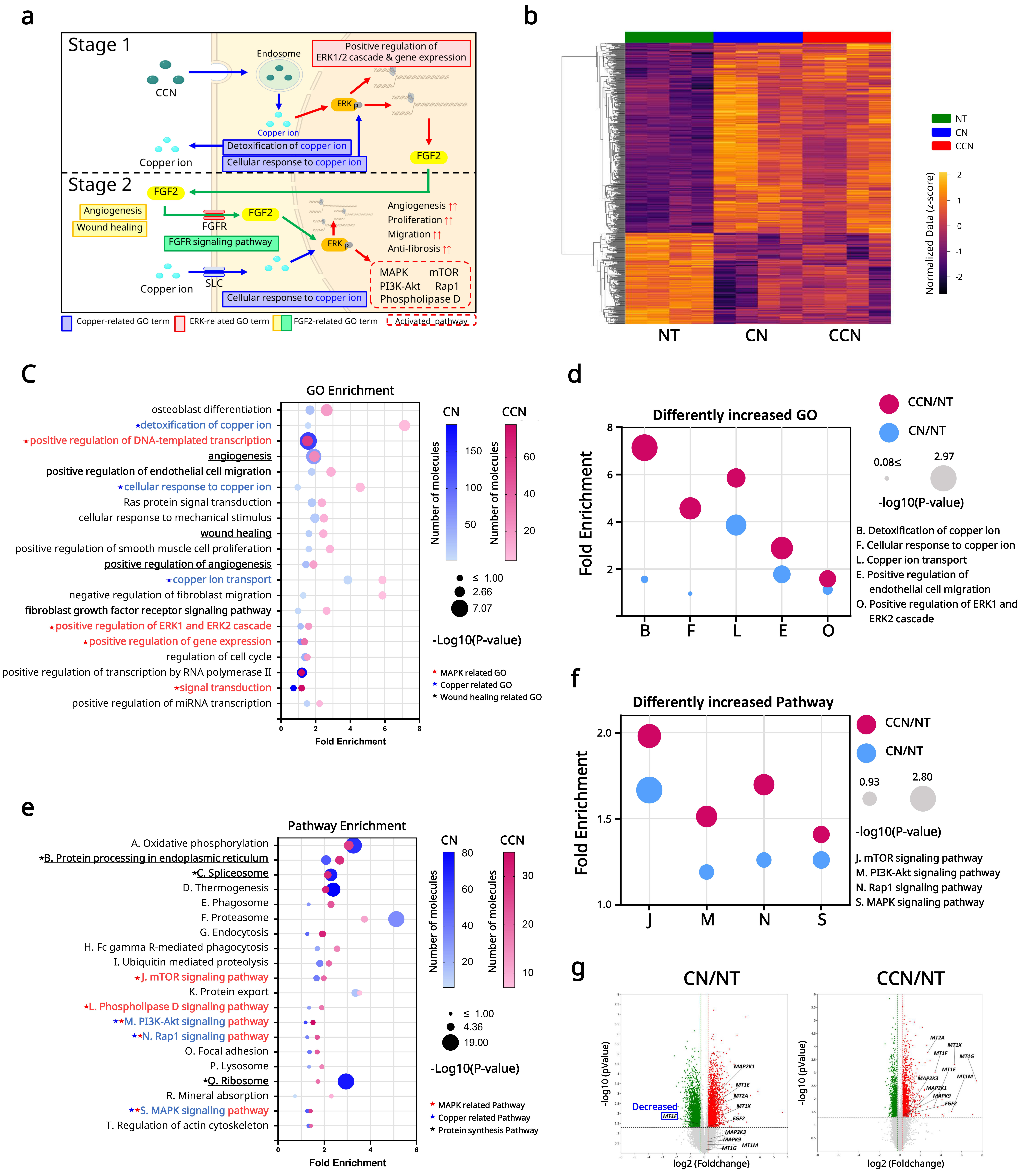
a
Stage 1
CCN
Endosome
Copper ion
Positive regulation of ERK1/2 cascade & gene expression
ERK
P
FGF2
Detoxification of copper ion
Cellular response to copper ion
Stage 2
FGF2
Angiogenesis
Wound healing
FGFR
FGFR signaling pathway
Angiogenesis ↑↑
Proliferation ↑↑
Migration ↑↑
Anti-fibrosis ↑↑
MAPK
mTOR
PI3K-Akt
Rap1
Phospholipase D
SLC
Copper-related GO term
ERK-related GO term
FGF2-related GO term
Activated pathway
b
NT
CN
CCN
Normalized Data (z-score)
2
1
0
-1
-2
C
GO Enrichment
osteoblast differentiation
★detoxification of copper ion
★positive regulation of DNA-templated transcription
angiogenesis
positive regulation of endothelial cell migration
★cellular response to copper ion
Ras protein signal transduction
cellular response to mechanical stimulus
wound healing
positive regulation of smooth muscle cell proliferation
positive regulation of angiogenesis
★copper ion transport
negative regulation of fibroblast migration
fibroblast growth factor receptor signaling pathway
★positive regulation of ERK1 and ERK2 cascade
★positive regulation of gene expression
regulation of cell cycle
positive regulation of transcription by RNA polymerase II
★signal transduction
positive regulation of miRNA transcription
Fold Enrichment
0
2
4
6
8
CN
CCN
Number of molecules
150
100
50
60
40
20
≤ 1.00
2.66
7.07
-Log10(P-value)
★ MAPK related GO
★ Copper related GO
★ Wound healing related GO
d
Differently increased GO
CCN/NT
CN/NT
0.08≤
2.97
-log10(P-value)
Fold Enrichment
8
6
4
2
B
F
L
E
O
B. Detoxification of copper ion
F. Cellular response to copper ion
L. Copper ion transport
E. Positive regulation of endothelial cell migration
O. Positive regulation of ERK1 and ERK2 cascade
e
Pathway Enrichment
A. Oxidative phosphorylation
★B. Protein processing in endoplasmic reticulum
★C. Spliceosome
D. Thermogenesis
E. Phagosome
F. Proteasome
G. Endocytosis
H. Fc gamma R-mediated phagocytosis
I. Ubiquitin mediated proteolysis
★J. mTOR signaling pathway
K. Protein export
★L. Phospholipase D signaling pathway
★★M. PI3K-Akt signaling pathway
★★N. Rap1 signaling pathway
O. Focal adhesion
P. Lysosome
★Q. Ribosome
R. Mineral absorption
★★S. MAPK signaling pathway
T. Regulation of actin cytoskeleton
Fold Enrichment
0
2
4
6
CN
CCN
Number of molecules
80
60
40
20
30
20
10
≤ 1.00
4.36
19.00
-Log10(P-value)
★ MAPK related Pathway
★ Copper related Pathway
★ Protein synthesis Pathway
f
Differently increased Pathway
CCN/NT
CN/NT
0.93
2.80
-log10(P-value)
Fold Enrichment
2.0
1.5
1.0
J
M
N
S
J. mTOR signaling pathway
M. PI3K-Akt signaling pathway
N. Rap1 signaling pathway
S. MAPK signaling pathway
g
CN/NT
CCN/NT
-log10 (pValue)
log2 (Foldchange)
Decreased
MT1F
MAP2K1
MT1E
MT2A
MT1X
FGF2
MAP2K3
MAPK9
MT1G
MT1M
MT2A
MT1X
MT1F
MT1G
MT1E
MAP2K3
MT1M
MAP2K1
MAPK9
FGF2

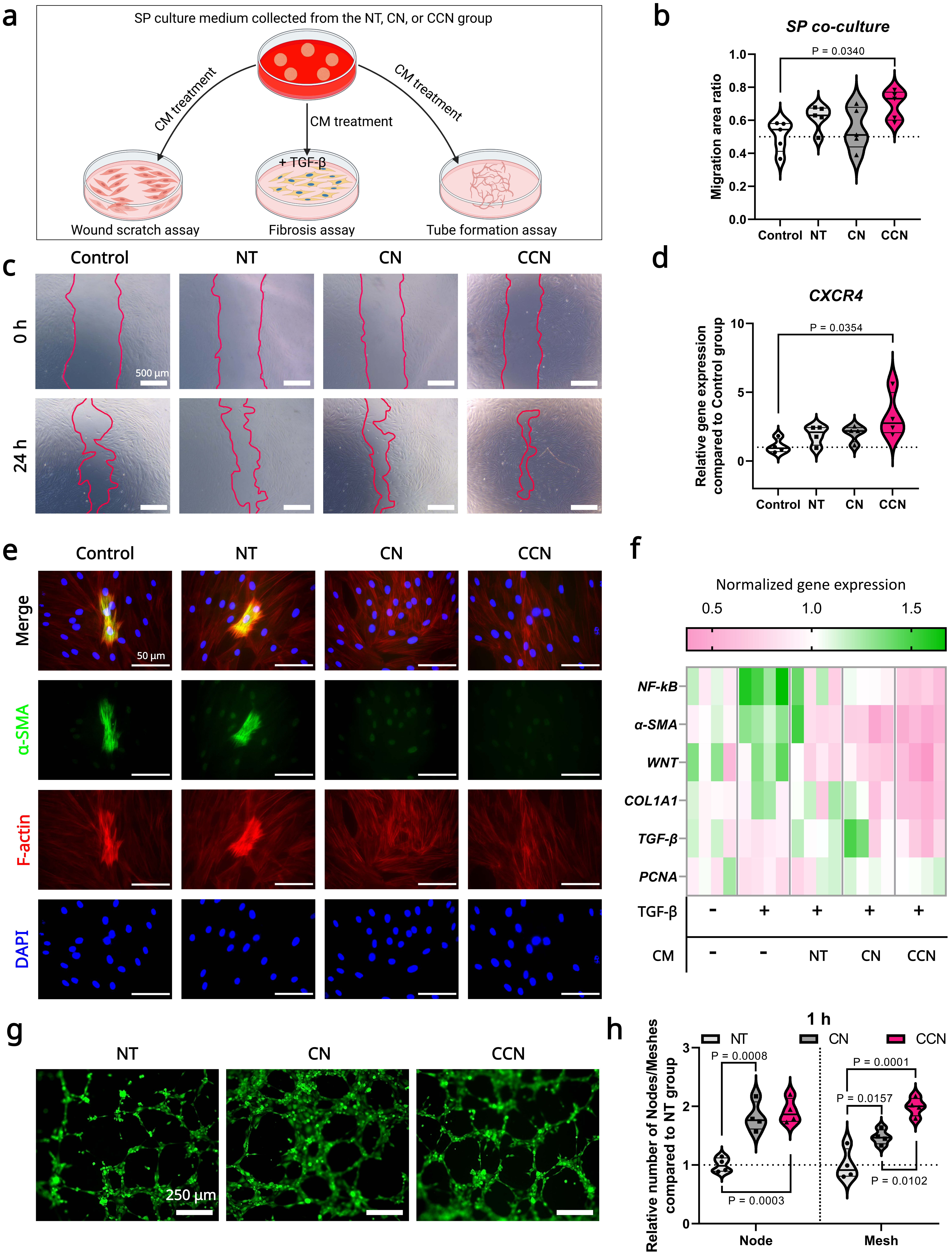
a
SP culture medium collected from the NT, CN, or CCN group
CM treatment
CM treatment
CM treatment
+ TGF-β
Wound scratch assay
Fibrosis assay
Tube formation assay
b
SP co-culture
P = 0.0340
Migration area ratio
1.0
0.8
0.6
0.4
0.2
0.0
Control
NT
CN
CCN
c
Control
NT
CN
CCN
0 h
24 h
500 µm
d
CXCR4
P = 0.0354
Relative gene expression compared to Control group
10
5
0
Control
NT
CN
CCN
e
Control
NT
CN
CCN
Merge
α-SMA
F-actin
DAPI
50 µm
f
Normalized gene expression
0.5
1.0
1.5
NF-kB
α-SMA
WNT
COL1A1
TGF-β
PCNA
TGF-β
-
+
+
+
+
CM
-
-
NT
CN
CCN
g
NT
CN
CCN
250 µm
h
1 h
NT
CN
CCN
P = 0.0008
P = 0.0003
P = 0.0001
P = 0.0157
P = 0.0102
Relative number of Nodes/Meshes compared to NT group
3
2
1
0
Node
Mesh